Performance Assessment of an Integrated Environmental Control System of Civil Hypersonic Vehicles

aerospace

MDPI

Article

Performance Assessment of an Integrated Environmental Control System of Civil Hypersonic Vehicles

Nicole Viola [1,*], Davide Ferretto [1], Roberta Fusaro [1] and Roberto Scigliano [2]

[1] Department of Mechanical and Aerospace Engineering, Politecnico di Torino, Corso Duca degli Abruzzi, 24, 10129 Turin, Italy; davide.ferretto@polito.it (D.F.); roberta.fusaro@polito.it (R.F.)
[2] Italian Aerospace Research Center (CIRA), Via Maiorise, 81043 Capua, Italy; r.scigliano@cira.it
* Correspondence: nicole.viola@polito.it

Abstract: This paper discloses the architecture and related performance of an environment control system designed to be integrated within a complex multi-functional thermal and energy management system that manages the heat loads and generation of electric power in a hypersonic vehicle by benefitting from the presence of cryogenic liquid hydrogen onboard. A bleed-less architecture implementing an open-loop cycle with a boot-strap sub-freezing air cycle machine is suggested. Hydrogen boil-off reveals to be a viable cold source for the heat exchangers of the system as well as for the convective insulation layer designed around the cabin walls. Including a 2 mm boil-off convective layer into the cabin cross-section proves to be far more effective than a more traditional air convective layer of approximately 60 mm. The application to STRATOFLY MR3, a Mach 8 waverider cruiser using liquid hydrogen as propellant, confirmed that presence of cryogenic tanks provides up to a 70% reduction in heat fluxes entering the cabin generated outside of it but inside the vehicle, by the propulsive system and other onboard systems. The effectiveness of the architecture was confirmed for all Mach numbers (from 0.3 to 8) and all flight altitudes (from sea level to 35 km).

Keywords: environmental control system; civil hypersonic vehicle; hydrogen boil-off; cabin system

Citation: Viola, N.; Ferretto, D.; Fusaro, R.; Scigliano, R. Performance Assessment of an Integrated Environmental Control System of Civil Hypersonic Vehicles. *Aerospace* **2022**, *9*, 201. https://doi.org/10.3390/aerospace9040201

Academic Editor: Bosko Rasuo

Received: 4 February 2022
Accepted: 29 March 2022
Published: 7 April 2022

1. Introduction

Hypersonic cruisers are currently considered the long-term future of long-range civil aviation. The expected high-level performance is challenging engineers and scientists from around the world in different technological and operational areas. Despite the wide range of solutions that are emerging for these challenges, it is widely agreed that there is an urgent need to improve the conceptual design stage, defining innovative and agile design methodologies able to capture all the most impacting design, performance, and operational characteristics since the beginning of the process and implementing multi-fidelity modeling strategies. The development of such an integrated methodology is one of the outcomes of the STRATOFLY Project, a Horizon 2020 Project funded by the European Commission in 2018, aimed at assessing the potential of this type of high-speed civil transport to reach TRL6 by 2035, with respect to key technological, societal, and economical aspects such as thermal and structural integrity, low-emissions combined propulsion cycles, subsystems design and integration including smart energy management, environmental aspects impacting climate change, noise emissions, and social acceptance and economic viability accounting for safety and human factors [1–3].

Among the technological challenges, thermal and energy management is one of the most critical for hypersonic vehicles. Thermal management is an example of significant interaction between onboard systems in subsonic aircraft, as it makes various systems (typically engine, fuel, electrical, hydraulic, and environmental control

systems) operate together to reject waste heat. In subsonic aircraft, heat exchangers spread across a range of systems use the aircraft fuel and ambient ram-air as heat sinks into which waste heat may be dumped [4]. The higher the performance of the aircraft, the more critical the issue of cooling down the system, rather than heating it up, and this happens because of the more complex avionics integrated onboard and because of the higher speed regime flown by the aircraft. The issue of thermal management becomes, therefore, more severe when the system is a high-speed aircraft, either supersonic or hypersonic. During high-speed flight, the aircraft is exposed to extremely high temperatures and heat fluxes as result of two phenomena: air stagnation and skin friction. At altitudes below 100 km, where the ambient pressure and density are significant, stagnation and viscous temperature effects are exacerbated. As a result, some of the most challenging thermal problems in aerospace vehicle design are encountered at the leading edges of hypersonic air-breathing vehicles.

Hypersonic vehicles are unique examples of highly integrated systems. To optimize hypersonic vehicles, not only aerothermodynamics, propulsion, and structure but also onboard systems have to be designed as closely interrelated. A crucial multidisciplinary integrated onboard system in hypersonic vehicles is the thermal and energy management system. Because of the high-speed flight and high-intensity combustion, hypersonic vehicles can provide enough high-quality heat source for power generation such as the aerodynamic heat and the combustion heat dissipation through engine walls [5]. Therefore, power-generation technology based on heat-to-electricity conversion through a closed thermodynamic cycle is appropriate for hypersonic vehicles. The cold source of the closed thermodynamic cycle cannot be ram-air in hypersonic flights. The fuel stored on board may act as cold source instead.

Many studies exist regarding hypersonic vehicles propelled by kerosene [6–8], methane [5], and liquid hydrogen [9–13]. Kerosene has lower gravimetric energy density than liquid hydrogen (40 MJ/kg for kerosene vs. 120 MJ/kg for liquid hydrogen) [14], which allows burning less mass of liquid hydrogen than kerosene to cover the same range while carrying the same number of passengers, thus keeping the take-off mass of the aircraft down. However, liquid hydrogen has a lower volumetric energy density than kerosene (10 MJ/L for liquid hydrogen vs. 35 MJ/L for kerosene) [14], which leads to bigger tanks to store liquid hydrogen on board and poses quite significant issues of integration to avoid the increase in drag of the vehicle's configuration. Generally, it can be stated that the properties of liquid methane lie in between kerosene and liquid hydrogen (50 MJ/kg and 25 MJ/L). On top of the technical properties of the different fuels, it is worth remembering that the environmental compatibility requirements will drive the design of future civil passenger aircrafts in all flight speed regimes. Keeping these constraints into account, especially in terms of pollutants and greenhouse gases emissions, both kerosene and liquid methane cannot meet the carbon neutral requirement and, for this reason, cannot pursue the Green Deal. Conversely, liquid hydrogen guarantees zero carbon dioxide emissions and lower nitrogen oxides emissions with respect to traditional fuel [15]. However, the advantage of liquid hydrogen from an environmental sustainability perspective shows drawbacks that cannot be neglected: a tremendous increase, with respect to traditional fuel [15], in water vapor emissions, which is not a pollutant but a greenhouse gas able to change the atmospheric composition and has a significant impact on climate [16–23]. Liquid hydrogen and sustainable aviation fuels (SAFs) seem to be the best alternatives to traditional fuels to propel high-speed aircraft, taking into account both technical performance and environmental compatibility requirements.

Future high-speed aircraft should, therefore, boost systems integration to enhance flexibility and safety, as shown by the thermal and energy management system (TEMS) on board the STRATOFLY MR3 vehicle, which includes the propulsive, fuel, thermal control, thermal protection, and electrical and environmental control systems [24].

Among the systems integrated into the TEM, the environmental control system (ECS) is surely the most power-demanding load for the pneumatic power on the aircraft, often requiring the highest secondary power load onboard (either pneumatic, in traditional architectures, or electrical, in bleed-less configurations). It is worth remembering that the ECS is a continuous request of pneumatic power throughout the flight [25].

The main functions of the ECS can be summarized as follows: (i) to maintain proper pressure levels within the cabin and systems compartments during all mission phases; (ii) to maintain proper temperature levels within the cabin and systems compartments during all mission phases; (iii) to maintain proper humidity levels and air chemical composition within the cabin (and system compartments where applicable) during all mission phases.

For high-speed aircraft, the requirements of the ECS are exacerbated by supersonic and hypersonic flight conditions, where advantage cannot be taken of the aircraft's skin or ram-air as heat sinks. The ECS of aircraft flying through the atmosphere at high-speed regimes must therefore comply with additional requirements, which lead to the following peculiar characteristics: (i) both ECS and dedicated thermal control systems (TCS) for thermal control may be used; (ii) depending on the flight speed, a thermal protection system (TPS) may be required as well; (iii) fuel and specifically cryogenic fuels may act both as coolant means and as heat rejection means; (iv) the complete set of thermal heat loads transfers is present (i.e., conduction, convection, and radiation); (v) hot and cold cases are quite different with respect to subsonic aircraft, where the cold case is generally represented by cruise condition at night and the hot case is represented by on ground conditions during a hot day.

Future high-speed aircraft need therefore to face new challenges to satisfy both performance and environmental requirements. Future aircraft, either subsonic, supersonic, or hypersonic, will be more digital, electrified, and integrated than their predecessors. High integration of different technologies to reach a highly multidisciplinary system will be pushed to the extremes for high-speed aircraft.

The paper focuses on the design and performance assessment of an innovative ECS for future hypersonic aircraft propelled by liquid hydrogen. The ECS was integrated within TEMS, the multidisciplinary system on board the vehicle that manages the heat loads and the generation of electric power through the exploitation of cryogenic liquid hydrogen [24]. The new technical solution was thoroughly investigated through detailed modeling and comprehensive analysis of the results. Comparisons with the architecture and performance of the A380, a state-of-the-art competitor of a hypersonic civil passenger aircraft, are shown. Finally, the main conclusions are drawn.

2. Reference Hypersonic Aircraft and Mission

The case study was the STRATOFLY MR3 vehicle, which is the result of research activities carried out by several international partners in the framework of the Horizon 2020 STRATOFLY Project funded by the EC since June 2018.

Aircraft Configuration and Mission Concept

Benefitting from the heritage of past European funded projects and, in particular, from the LAPCAT II project led by ESA [11–26], the waverider configuration was adopted and investigated in-depth throughout all flight phases. The STARTOFLY MR3 is a highly integrated system, where propulsion, aerothermodynamics, structures, and onboard systems are strictly interrelated to one another as highlighted in Figure 1 [2,3].

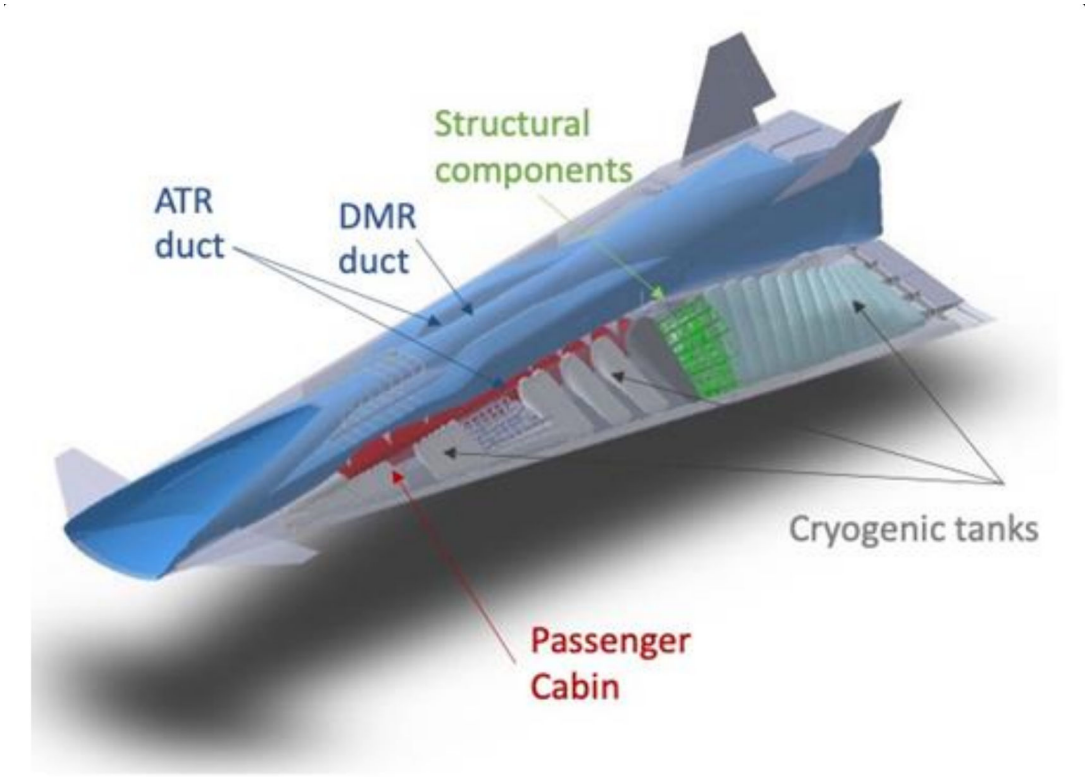

Figure 1. STRATOFLY MR3 vehicle with indication of main subsystems.

The STRATOFLY MR3 vehicle's design was driven by its peculiar mission concept that can be summarized as follows: the STRATOFLY MR3 is able to fly along long-haul antipodal routes reaching Mach 8 during the cruise phase at a stratospheric altitude (h > 30,000 m), carrying 300 passengers as payload. The STRATOFLY MR3 has a waverider configuration to maximize aerodynamic efficiency and improve range performance. Unlike many waverider concepts, STRATOFLY MR3 has engines and related air ducts embedded into the airframe and located at the top of the vehicle to increase the available planform for lift generation without additional drag penalties, thus further improving the aerodynamic efficiency. In addition, this configuration allows optimizing the internal volume and guarantees to expand the jet to a large exit nozzle area without the need to perturb the external shape, which would lead to extra pressure drag.

The mission profile (Figure 2a) was based on the LAPCAT reference mission [27]. At the beginning of the mission, the air turbo rocket (ATR) engines were turned on and the vehicle performed the first climb phase, which terminated at Mach = 0.95 at an altitude between 11 and 13 km. The ATR is a turbine-based combined cycle engine, which brings together elements of the turbojet and rocket motors and provides a unique set of performance. This engine has, in fact, a high thrust-to-weight ratio and specific thrust over a wide range of speed and altitude, thus representing an excellent choice as an accelerator engine up to high supersonic speeds. Then, the vehicle performed the subsonic cruise to prevent a sonic boom while flying over land. After the subsonic cruise, the super-sonic climb started, and the vehicle accelerated up to Mach 4. At the end of this phase, the ATR engines were turned off and the dual mode ramjet (DMR) was activated to accelerate to Mach 8, during the hypersonic climb. The DMR is the high-speed engine that can operate in both the ramjet and scramjet modes of operations. The next phase, immediately after the hypersonic climb, was the hypersonic cruise at an altitude between 30 and 35 km (Figure 2b). Eventually, the engines were turned off and the vehicle performed the descent towards the landing site.

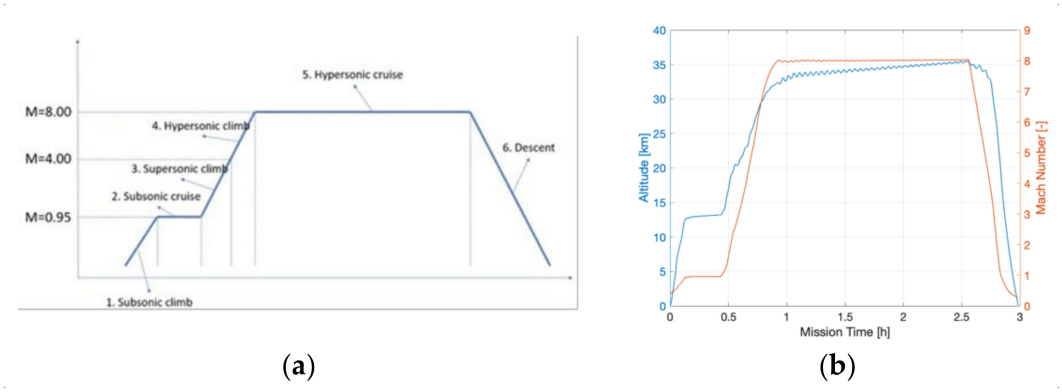

Figure 2. (**a**) STARTOFLY MR3 mission profile; (**b**) STRATOFLY MR3 flight altitude (light blue) and Mach number (orange) versus mission time.

Main technical data for the STRATOFLY MR3 are reported in Table 1.

Table 1. Main technical data for the STRATOFLY MR3.

Technical Data	Value	Unit of Measurement
Length, l	94	m
Wingspan, 2b	41	m
Height, H	17	m
Maximum take-off weight, MTOW	400	tons
Overall volume, V	10,000	m^3
Fuel weight, W_f	200	tons
Maximum thrust at take-off, T_{to}	3070	kN
Thrust during cruise, T_c	500	kN

The waverider configuration of the STRATOFLY MR3 is dominated by the engines and their related air ducts, which stretch from the front (air inlet) to the rear of the vehicle (nozzle). The aircraft is equipped with six ATR engines and one DMR engine. The propulsive system is embedded into the lightweight bubble structure of the aircraft to optimize aerodynamic and maximize internal volume for onboard systems. The passenger cabin is located beneath the engines' combustor at the bottom of the vehicle, and it is surrounded by liquid hydrogen tanks. The aircraft is a unique example of highly integrated systems, as testified to by the thermal and energy management system, which integrates propulsive, fuel, thermal control, thermal protection, and electrical and environmental control systems. Figure 3 shows the TEM system. The heat loads which penetrate the aeroshell generate boil-off within the cryogenic tanks. The boil-off line (cyan line in Figure 3) collects hydrogen vapors from the different tanks to use boil-off hydrogen as coolant mean for different loads prior to being injected into the combustion chamber of the propulsion plant. The liquid hydrogen line (blue line in Figure 3) transfers the propellant from the auxiliary tanks to the primary ones to feed the engines. The high-pressure liquid hydrogen cools the propulsion plant in the cooling jacket, and it is then expanded through a turbine to provide mechanical power and, subsequently, electrical power. The turbine drives, in fact, both the boil-off compressor and the electrical generator.

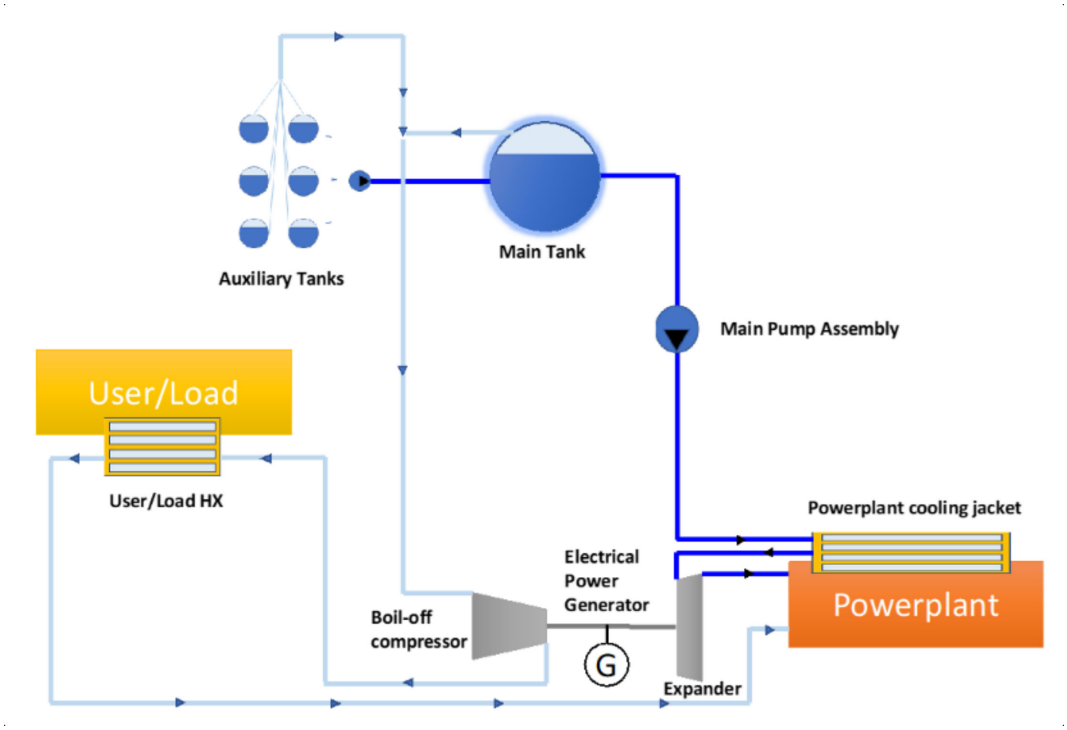

Figure 3. Thermal and energy management system on board the STRATOFLY MR3.

3. Environmental Control System Design: Architecture and Mathematical Modeling

Among the systems integrated into the TEM, the environmental control system is the most power-demanding load for the pneumatic power on the aircraft, often requiring the highest secondary power load onboard throughout the flight.

3.1. ECS Architecture

Traditionally, engine bleed-air strategy has been used to obtain high-pressure, high-temperature air from engine compressor stages to feed the ECS. Concorde adopted this approach, bleeding the air off the last stage of the high-pressure compressor of the engines. Tapping bleed-air off the engine compressor is extremely wasteful, especially as engine pressure ratios and bypass ratios increase in modern engines. Evidently, engine compressor bleed-air configuration is fuel inefficient in supersonic speed regimes and energy-efficient engines [25].

No-bleed systems architecture allows the airplane's engines to produce thrust more efficiently, as all the high-speed air produced by the engines goes to thrust. For this reason, recent architectures aim at overcoming the need for the engine bleed, pursuing the so-called bleed-less configuration. This is the typical architecture of more-electric aircraft (MEA) concepts, where the high-pressure, high-temperature air is provided by ram-air compressed by dedicated compressors driven by electrical motor, thus completely separated from the propulsive plant. The design of supersonic ram-air inlets for the electrical motor-driven compressors would require careful attention, but shock inlets could provide the required subsonic airflow without too much loo in ram recovery.

Comparisons between the pressure and temperature values of the bleed-air extracted by the ATR engine and the ram-air extracted by the engine inlet duct are shown in Figures 4 and 5. These values have been extracted from CFD analyses by the experts of the propulsion system as part of the research activity carried out in the framework of the H2020 STRATOFLY Project. Figure 4a,b depict the conditions of the traditional bleed configuration, whereas Figure 5a,b depict the conditions of the innovative bleed-less configuration. Both the pressure and temperature values of the bleed-less configuration are lower with respect to those of the bleed configuration as expected. The STRATOFLY MR3 adopts a bleed-less architecture with a dedicated compressor to increase the pressure and temperature of

the ram-air extracted by the engine inlet duct up to the required values. Detailed analyses should be performed to estimate the impact of ram-air extraction on the propulsive system's performance.

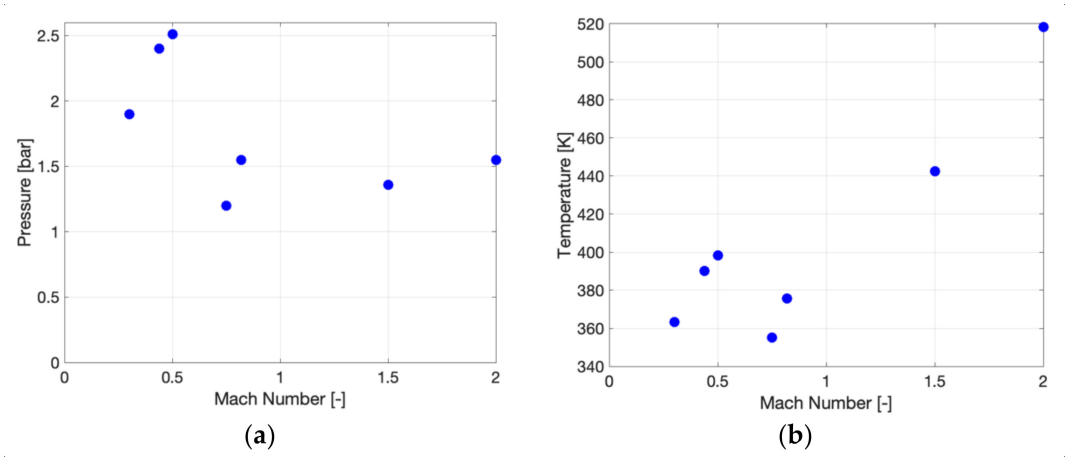

Figure 4. (**a**) Pressure versus Mach of the bleed-air (ATR engine); (**b**) temperature versus Mach of the bleed-air (ATR engine).

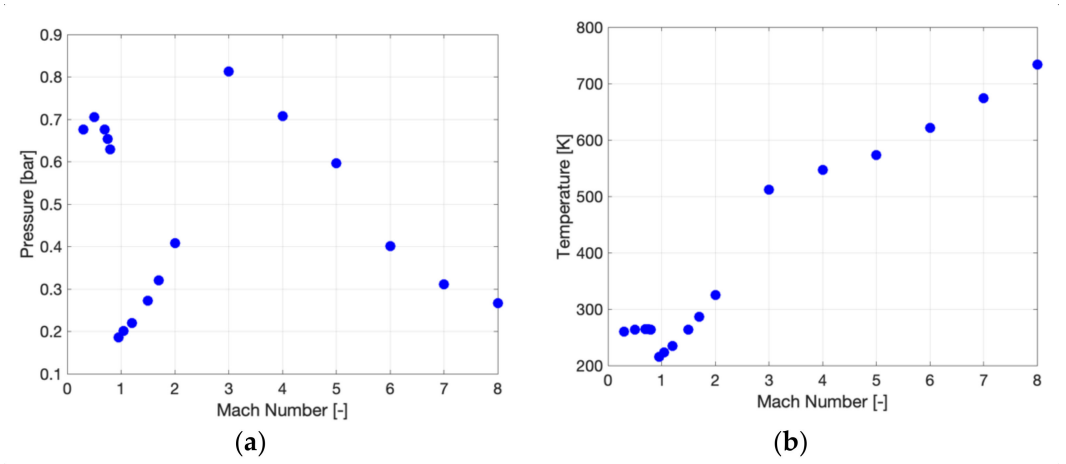

Figure 5. (**a**) Pressure versus Mach of ram-air; (**b**) temperature versus Mach of the ram-air.

The air mass flow, extracted by the engine air intake, is then regulated through the cold air unit (CAU), which regulates the pressure and temperature of the air to meet the cabin requirements. In the open-loop architecture, selected for the ECS of the STRATOFLY MR3, an outflow valve regulates the air discharged outside the aircraft and additional relief valves balance the inside and outside pressures in all conditions. The CAU is an air cycle machine with a bootstrap sub-freezing architecture (Figure 6a). A dedicated auxiliary compressor, driven by an electric motor, was integrated ahead of the primary heat exchanger of the CAU to reach the necessary air pressure level to finally comply with the requirements of air pressure and air temperature at the CAU's exit. Figure 6b shows the variation with Mach number of the pressure of the ram-air extracted by the engine inlet duct and of the air entering the CAU's compressor. It is clear that the auxiliary compressor was needed to increase the ram-air pressure level to comply with the required air pressure values when entering the CAU's compressor.

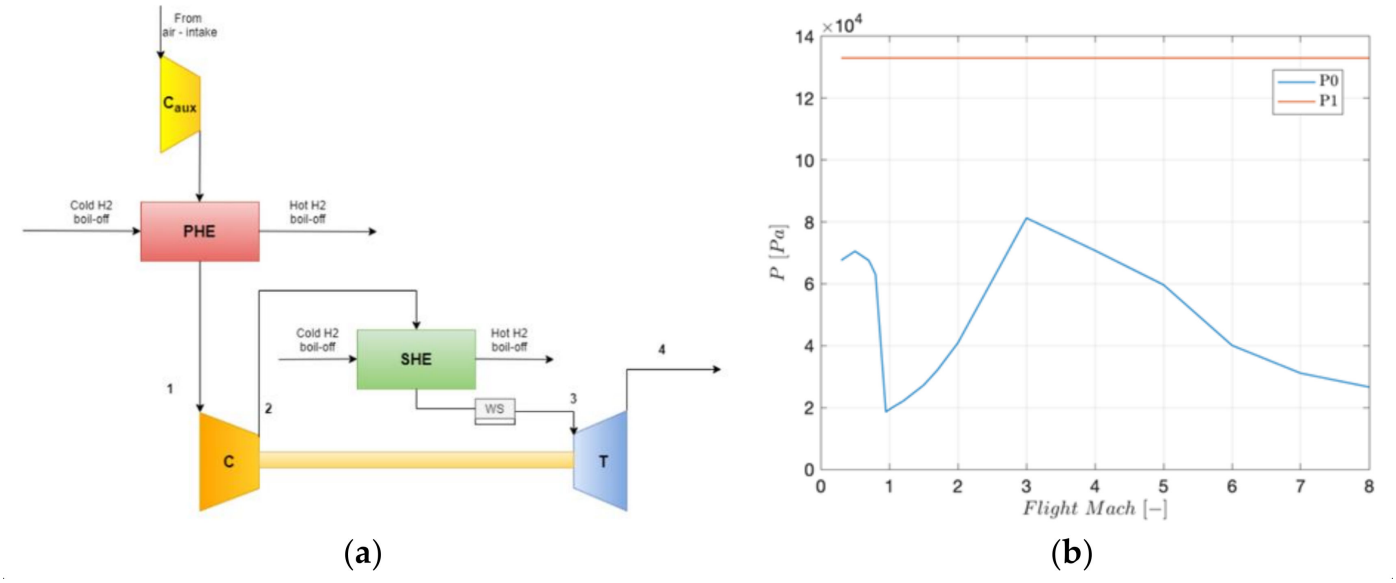

Figure 6. (**a**) Bootstrap sub-freezing air cycle machine CAU with an auxiliary compressor (C_{aux}), a primary heat exchanger (PHE), a secondary heat exchanger (SHE), a water separator (WS), a compressor (C), and a turbine (T); (**b**) variation of the pressure of the ram-air extracted by the engine inlet duct (p_0) and of the air entering the CAU's compressor (p_1) with Mach number.

Figure 7 shows two different modes of operations of the CAU: the cold case and the hot case. In the cold case, when the cabin needs to be warmed up, the by-pass line is activated, and the air extracted from the engine air intake is mixed with the air flow exiting from the CAU. Before entering the cabin, the air flow is also mixed with the air recirculating from the cabin itself. In the hot case, when the cabin needs to be cooled down, no by-pass mass flow is required, and the air mass flow exiting from the CAU is mixed only with the air recirculating from the cabin, before entering the cabin itself.

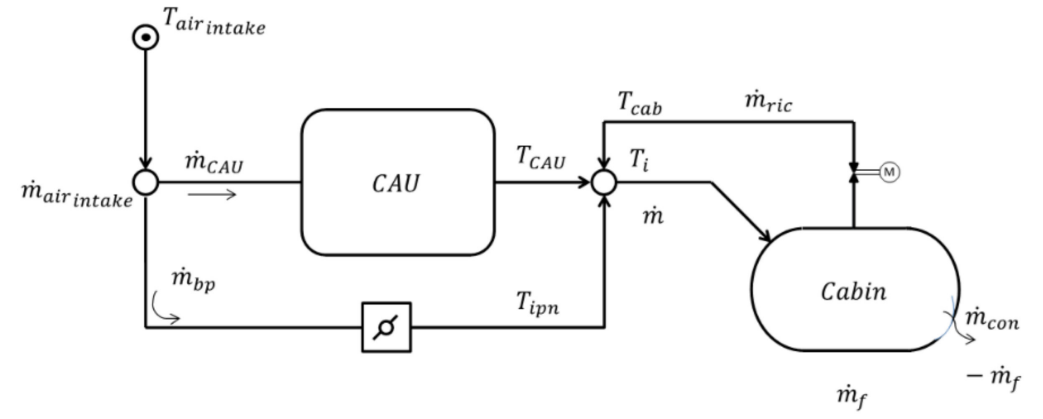

Figure 7. Bootstrap sub-freezing CAU in two different modes of operations: the cold case and the hot case.

3.2. ECS Mathematical Modeling

Depending on the environmental conditions, the modes of operations of the aircraft (particularly, the engine-on and engine-off conditions) and the configurations of the cabin (empty cabin or full of passengers), different scenarios can be defined: (i) cold case scenario, when the external environment either outside the aircraft or outside the cabin is cold and it is therefore necessary to warm up the cabin; (ii) hot case scenario, when the ex-ternal environment either outside the aircraft or outside the cabin is warm and it is therefore necessary to cool down the cabin.

The CAU should manage the inwards/outwards heat fluxes by providing the cabin with the correct air mass flow to comply with requirements.

The cabin temperature should range between 291 (18 °C) and 298 K (25 °C). CS-25 prescribes that pressurized cabins should be equipped to provide a cabin pressure altitude of no more than 2438 m (8000 ft) at the maximum operating altitude of the aircraft under nominal operating conditions. The higher the altitude simulated within the cabin during cruise, the better it is for the structure, due to the lower differential pressure values be-tween the outer atmosphere and inner environment. A compromise should therefore be reached between passengers' comfort and structural performance. In addition to temperature and pressure requirements, CS-25 prescribes that each passenger and crew compartment should be ventilated, and each crew compartment should have enough fresh air to enable crewmembers to perform their duties without undue discomfort or fatigue, being not less than 0.28 m^3/min (0.343 kg/min or 5.7 g/s). The supply of fresh air in the event of loss of one source should not be less than 0.147 m^3/min (0.18 kg/min or 3 g/s) for any period exceeding five minutes.

In cold case scenarios (Figure 8), the ECS should provide the cabin with hot air mass flow to balance the outward heat fluxes. If the ECS was not active, the heat load would increase, and T_{cab} would reach unacceptable values (T_{cab} < 18 °C). A typical temperature value of the hot air mass flow entering the cabin is T_i = 50 °C, and the target temperature of the cabin is T_{cab} = 18 °C.

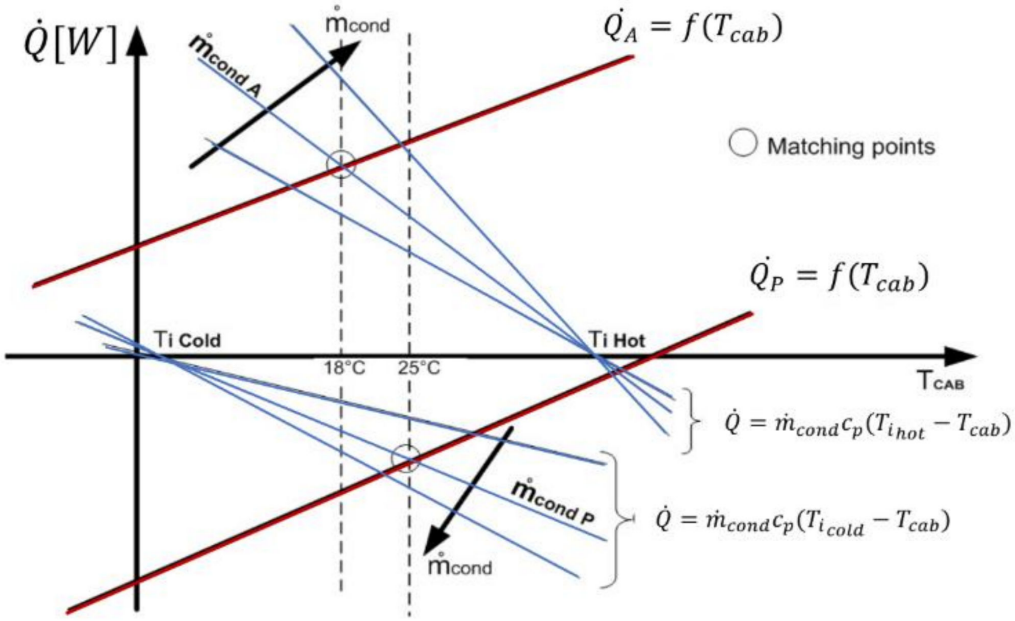

Figure 8. Cold and hot cases.

In hot case scenarios (Figure 8), the ECS should provide the cabin with cold air mass flow to balance inward heat fluxes. If the ECS was not active, the heat load would decrease and the temperature of the cabin, T_{cab}, would reach unacceptable values (T_{cab} > 25 °C). A typical temperature value of the cold air mass flow entering the cabin is Ti = 2 °C, and the target temperature of the cabin is T_{cab} = 25 °C. In Figure 8, the red lines represent the variation of the heat load with the temperature inside the cabin for the cold and hot case scenarios, while the blue lines depict the heat load supplied by the ECS. Depending on the desired cabin temperature, different values of air mass flow are required and, consequently, different heat loads provided by the ECS.

The mathematical relationship that expresses the heat load that the ECS should provide as a function of the desired cabin temperature with varying air mass flow is reported hereafter:

$$\dot{Q} = \dot{m} c_p (T_i - T_{cab}) \tag{1}$$

The air mass flow that the ECS should supply is therefore given by Equation (2), which reports also the values of the temperature of the air entering the cabin and the temperature of the air inside the cabin for the hot and the cold cases:

$$\dot{m} = \frac{\dot{Q}}{c_p (T_i - T_{cab})} \quad T_i = \left\{ \begin{array}{c} 2\,^{\circ}C - 6\,^{\circ}C \; hot \; case \\ 40\,^{\circ}C - 50\,^{\circ}C \; cold \; case \end{array} \right\} \quad T_{cab} = \left\{ \begin{array}{c} 25\,^{\circ}C \; hot \; case \\ 18\,^{\circ}C \; cold \; case \end{array} \right\} \tag{2}$$

Table 2 summarizes some of the different scenarios that hypersonic vehicles can face. Unlike subsonic civil passenger aircraft that experience the cold case scenario in cruise, during cold nights, without passengers (load factor equal to zero, during transfers), hypersonic civil passenger aircraft experience the cold case scenario either when parking on ground, in the engine-off mode of operation, without passengers on board, or in the sub-sonic climb/cruise phases at 5000–10,000 m of altitude without passengers. Conversely, while the hot case for subsonic civil passenger aircraft happens on-ground, during hot days with passengers at full capacity (load factor equal to 1), and for hypersonic aircraft, it occurs in cruise phase (Mach 8 for the. STRATOFLY MR3), in the engine-on mode of operation with passengers at full capacity. Table 2 lists only nominal conditions. Out-of-nominal conditions are further investigated.

Table 2. Cold and hot cases for hypersonic vehicles (nominal conditions).

Condition ID	ISA Specification	Time of the Day	Mission Phase	Modes of Operations	Load Factor	Comments
1	ISA on ground (cold)	Night	Parking	Engine-off	0	COLD CASE
2	ISA	Night	Subsonic cruise	Engine-on	0.5	Typical
...	...	...	...		...	...
n−1	ISA	Day	Landing	Engine-on Limited amount of LH2	1 (full capacity)	To be investigated
n	ISA at 30 Km altitude	Day	Cruise	Engine-on	1 (full capacity)	HOT CASE

From preliminary investigations, the worst-case scenario for hypersonic vehicles is the hot case, when the aircraft is flying at hypersonic speed, ranging, in the case of the STRATOFLY MR3, from Mach 4 to Mach 8.

Three types of heat loads can be determined at hypersonic speed as reported in Equation (3):

- External heat load acting on the external skin: these heat loads are external to the vehicle;
- Internal heat load generated inside the cabin: these heat loads are internal to the vehicle and internal to the cabin;
- Internal heat load acting on the external skin of the cabin: these heat loads are internal to the vehicle but external to the cabin.

$$\dot{Q} = \dot{Q}_{external} + \dot{Q}_{internal\_cab} + \dot{Q}_{external\_cab} \tag{3}$$

Unlike subsonic civil passenger aircraft, which should withstand only external and internal heat loads, hypersonic aircraft are also subject to internal heat loads acting on the external shell of the cabin because of their innovative and highly integrated configuration with embedded high-speed propulsion.

3.2.1. Mathematical Modeling of External Heat Loads

To assess the external heat load transfer (i.e., heat fluxes (W/m^2)), first the wall temperature, Tw, was calculated through a zero-dimensional steady-state analysis based upon the convective–radiative–conductive heat transfer balance [27] as shown in Equation (4):

$$h_{conv}(T_{rec} - T_w) = \varepsilon\sigma T_w^4 + \frac{k}{t}(T_w - T_{LH2}) \quad (4)$$

Hereafter, the reader can find suggestions for a generic hypersonic vehicle:

- The external geometry of the vehicle can be simplified as a set of inclined flat plates;
- The thermal conductivity, k, can be estimated equal to 1 W/(mK) [26], considering the insulation material of the tanks based upon quartz fiber;
- The thickness of the skin (including insulation layer), t, is usually set equal to 0.1 m;
- The internal side of panels has an insulation layer that is in contact with the cryogenic liquid hydrogen tank at 20 K. This simplifying hypothesis clearly holds true only for some compartments of the vehicle. A more detailed analysis that considers the two different types of vehicle's compartment, i.e., those that have the external skin in contact with LH2 tanks and those that do not have the external skin in contact with LH2 tanks should be carried out as future research activity;
- The following values of emissivity, ε, have been considered for different high-temperature materials for the TPS-panels of the skin: ε = 0.3 for metallic alloys (Inconel, Titanium); ε = 0.8 for ceramic materials (C/C, C/SiC); ε = 1.0 for the ideal upper limit.

The convective heat transfer coefficient, h_{conv}, is expressed by Equation (5), where the specific heat at a constant pressure is set equal to $c_p = 1400.5\frac{J}{kg\ K}$:

$$h_{conv} = S_t \rho_\infty v_\infty c_p \quad (5)$$

The mathematical relationship of the Stanton number, S_t, is reported in Equation (6):

$$S_t = \frac{c_f}{2{\cdot}0.95} \quad (6)$$

The turbulent skin friction coefficient, c_f, is given by Equations (7)–(9):

$$c_f = \frac{0.0583}{Re_x^{0.2}}\left(\frac{T_\infty}{T_{ref}}\right)^{0.8}\left(\frac{\mu_{ref}}{\mu_\infty}\right)^{0.2} \quad (7)$$

$$\frac{T_{ref}}{T_\infty} = 0.5\left(1 + \frac{T_w}{T_\infty}\right) + 0.22\left(\frac{T_{rec}}{T_\infty} - 1\right) \quad (8)$$

$$T_{rec} = T_\infty\left(1 + R\frac{\gamma - 1}{2}M_\infty^2\right) \quad (9)$$

$$R = Pr^{1/3}, \quad (10)$$

The convective heat transfer is estimated equal to 450 $W/(m^2K)$ for aircraft that cruise at Mach 8. The external heat load transfer is thus calculated as follows (Equation (11)):

$$\dot{q}_{external} = h_{conv}(T_{rec} - T_w) \quad (11)$$

3.2.2. Mathematical Modeling of Heat Loads Generated Inside the Cabin

The internal heat loads are the sum of heat loads due to the metabolism (human beings) and to the onboard systems:

$$\dot{Q}_{internal\_cab} = \dot{Q}_{met} + \dot{Q}_{sys\_int} \quad (12)$$

The heat load generated by the metabolism is expressed by Equation (13):

$$\dot{Q}_{met} = \dot{Q}_{rest} n_{pax} + \dot{Q}_{work} n_{crew} \quad (13)$$

The heat load generated by human bodies at rest is estimated to be equal to $\dot{Q}_{\text{rest}} = 100$ W, while the heat load produced by human bodies at work is estimated to be equal to $\dot{Q}_{\text{work}} = 300$ W. The number of passengers carried on board the STRATOFLY MR3 is $n_{pax} = 300$, and the estimated number of crew members in the cockpit and in the cabin is equal to $n_{crew} = 12$.

The heat loads generated by the avionic equipment installed inside the cabin and usually related to the passengers' comfort cannot be estimated through statistical models available for subsonic aircraft. Indeed, with respect to subsonic aircraft, the adoption of a windowless cabin configuration may, for example, lead to an increase in the electric power demand of avionic equipment and, consequently, to the generated heat loads. However, the technologies' enhancement in cooling capabilities (e.g., integrated boil-off hydrogen heat exchangers and heat-pipes) of the avionic equipment can yield a reduction up to 20% of the expected heat loads inside the cabin (K_{eq}).

Therefore, the heat load produced by onboard systems inside the cabin ($\dot{Q}_{sys\_int}$) is expressed as function of the electric power demand of the cabin onboard equipment (Equation (14)), $\dot{Q}_{pax\_eq}$ (cabin compartment contribution in Figure 9), where the coefficient K_{eq} is equal to 0.8:

$$\dot{Q}_{sys\_int} = \left(\dot{Q}_{pax\_eq}\right) K_{eq} \quad (14)$$

Making benefit of the detailed analyses and simulations performed in the framework of the H2020 STRATOFLY Project for the sizing and integration of onboard systems of the STRATOFLY MR3, an electric power demand of approximately 200 kW for the entire cabin compartment as considered ($\dot{Q}_{pax\_eq}$). Therefore, a value of 160 kW for $\dot{Q}_{sys\_int}$ is here suggested for a hypersonic vehicle carrying 300 pax.

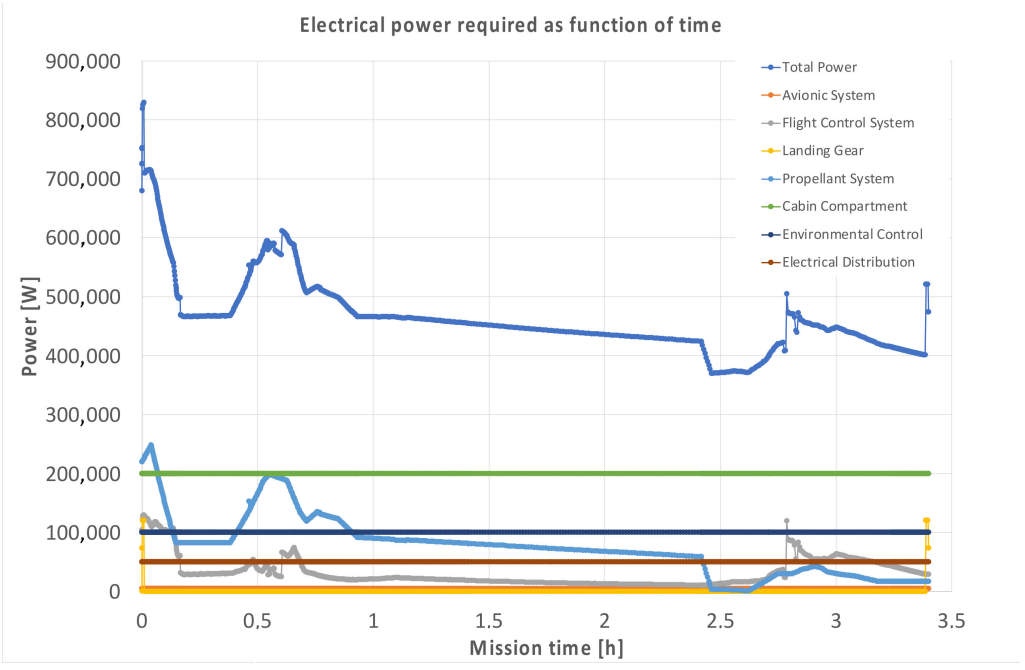

Figure 9. STRATOFLY MR3 power budget.

3.2.3. Mathematical Modeling of Heat Loads Generated Outside the Cabin

There are heat loads that are generated inside the vehicle but act on the external skin of the cabin ($(\dot{Q}_{cab\ top})_{cond}$). Typical examples are the loads coming from the engine compartment ($\left[(\dot{Q}_{cab\ top})_{cond}\right]_{eng}$) and those generated by all subsystems installed on the aircraft but externally to the cabin ($\left[(\dot{Q}_{cab\ top})_{cond}\right]_{subsys}$). Complementary, the bottom of the cabin usually lies on the ventral skin of the aircraft along its entire length, which is exposed to $(\dot{Q}_{cab\ bottom})_{cond}$. The front and rear sides of the cabin, as well as the lateral side of most cabin's compartments interface with liquid hydrogen tanks (Figure 10a). The rear side of the cabin is not directly connected to liquid hydrogen tanks because of the landing gear retraction bay, but this contribution can be neglected. All cabin sides that interface with hydrogen tanks are considered isolated from the external environment; their contribution to the total incoming heat flow can thus be neglected.

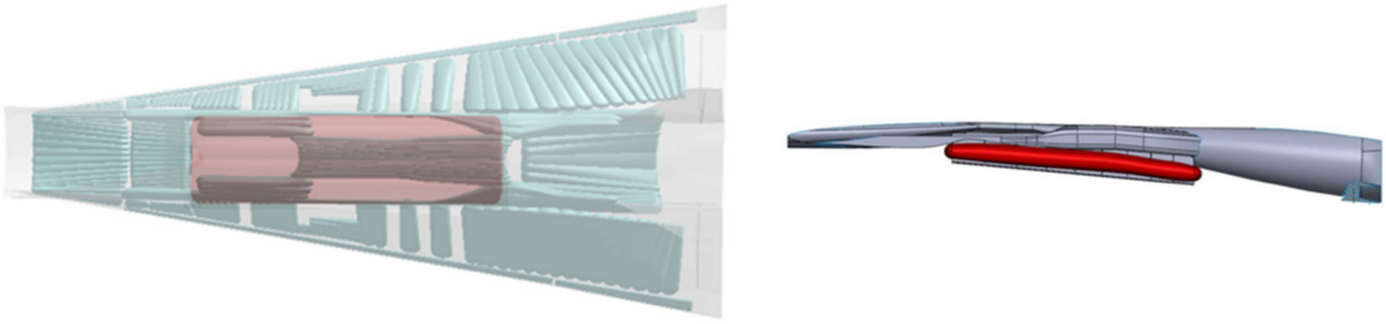

(a) **(b)**

Figure 10. (**a**) Top view of the STRATOFLY MR3 and the cabin; (**b**) side view of the STRATOFLY MR3 and the cabin.

As far as the heat loads generated by the engine compartment are concerned, it is very important to understand the location and the mutual interfaces between the entire propulsive path (which includes the inlet, combustion chambers, and nozzle) and the cabin compartment. To meet mission requirements, the propulsive system of a hypersonic vehicle can be impressively long, and the aircraft concept built around it. A clear example is shown by the STRATOFLY MR3 concept, where the integrated propulsive subsystem extends for the entire length of the vehicle (Figure 10b). In this case, to properly assess the temperature distributions and the thermal power due to the presence of the engines, a detailed thermal analysis was carried out. In detail, the internal configuration of the cabin consists of six passenger compartments at different floor levels and with different passenger capacities (300 first class seats), one cockpit with two pilots, stairs, lavatories, and galleys, as shown in Figure 11, where the main technical data are reported. The cabin is thus modeled as a structure composed of seven single adjacent compartments between which the heat load transfer is neglected. The cabin ceiling is mechanically connected to the propulsive system bay through an aluminum reticular metal structure and each section of the cabin compartment interface with different areas of the propulsive flow-path.

For each compartment, a set of control points were identified (Figure 12). The first set of thermal simulations was carried out to verify a preliminary hypothesis of homogeneous temperature distribution along the cabin wall. These first simulations, even if carried out using a simplified model with no cryogenic tanks onboard, confirmed that the hypothesis was not applicable. The simulations revealed that the maximum average temperatures reached at the top external wall of the cabin

exceeded 1000 °C. However, this result has been achieved without considering the integration of the liquid hydrogen tanks and the propellant depletion throughout the mission. Therefore, a second set of simulations with detailed modeling of cryogenic tanks and their internal temperature evolution along the mission (depending on the amount of residual fuel in each of them) was carried out. The results of this final set of simulations are reported in Figure 13, where it is clearly visible that the last three compartments, located close to the nozzle structure, are those for which the highest temperatures are experienced throughout the reference mission profile. As expected, the highest temperatures were reached when the aircraft was slowing down during the descent phase because of the heat load accumulated during the entire trajectory. However, the maximum pick temperature reached was considerably lower than the one estimated in the first set of simulations. Therefore, it is possible to assert that the massive presence of cryogenic propellant on board can contribute to lower the temperatures inside the vehicle and, consequently, the heat fluxes entering the cabin up to 70%.

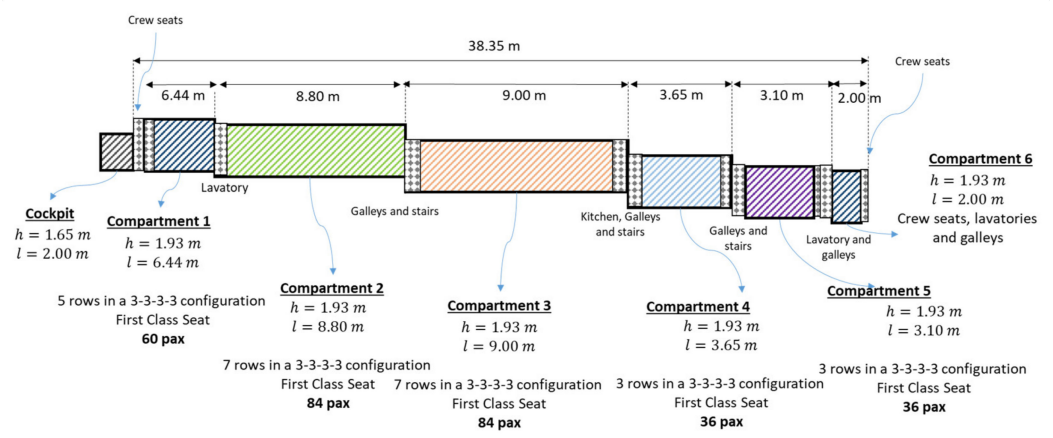

Figure 11. Artistic impression of the passenger cabin with main configuration data.

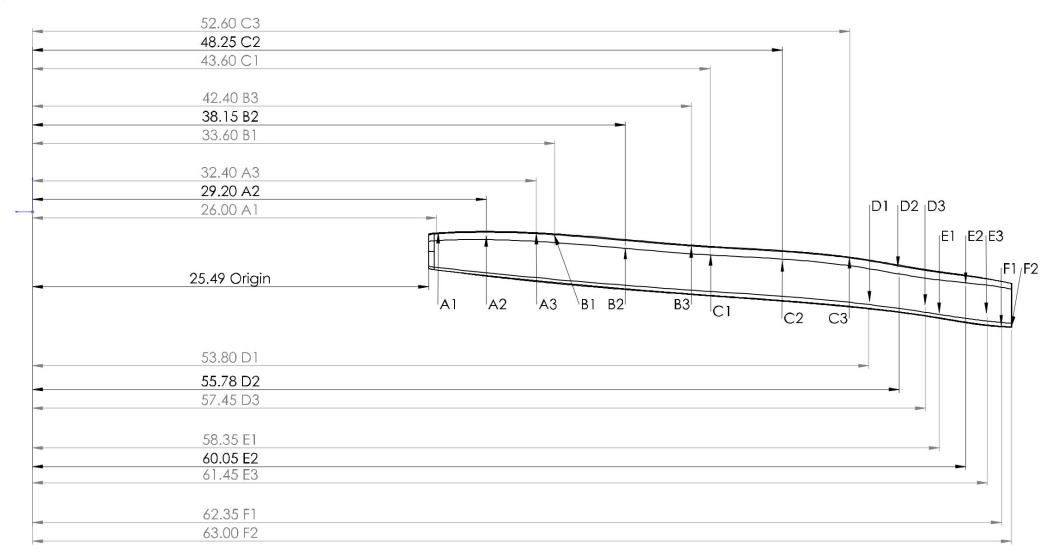

Figure 12. Lateral view of the passenger cabin with indication of the heat load measurement points identified per each compartment.

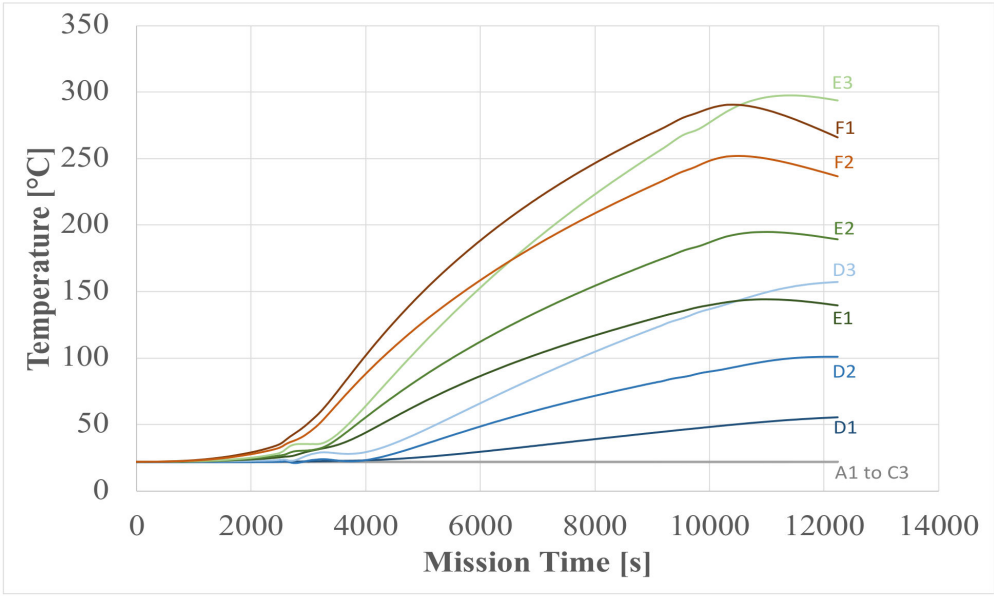

Figure 13. Temperature profiles insisting on top of the passenger cabin and due to the presence of the propulsive flow-path (T_{eng}).

Once the temperature profile due to the presence of the engine was known, the thicknesses and conductivities of the layers' materials of the cabin were assessed to estimate the incoming heat fluxes into the cabin.

As far as the contributions of the other subsystems ($\dot{Q}_{eq}$) were concerned, as a rule of thumb, the expected heat loads coming from the subsystems equaled their electric power demand. However, estimations of the $\dot{Q}_{eq}$ were significantly different for the subsonic and hypersonic aircraft, because of the following reasons: (i) difference between subsonic and hypersonic aircraft in the electric power demand of onboard subsystems; (ii) the expected enhancement in self-contained cooling capabilities of the onboard subsystems in hypersonic aircraft due to the overall vehicle configuration with cryogenic fuel tanks, and (iii) the enhanced cooling performance of the cabin cross-sectional configuration in hypersonic aircraft. Therefore, making benefit of the detailed thermal analysis and simulations performed in the framework of the H2020 STRATOFLY Project, the $\dot{Q}_{eq}$ values were updated. Specifically, considering that for the MR3, hosting 300 pax, an average electrical power demand of 200 kW for all onboard subsystems other than the cabin was requested, and assuming that the massive presence of cryogenic tanks can lead to a reduction of up to 70%, as a preliminary estimation of the expected heat load acting onto the cabin, the onboard subsystems contribution ($\dot{Q}_{eq}$) can be estimated to be 60 kW for a 300 pax aircraft. Complementary, as a first hypothesis, the lateral sides of the cross–section of each cabin compartment were considered isolated from the outside of the cabin thanks to the interface with hydrogen tanks (Figure 14).

3.2.4. Cabin Wall Modeling and Heat Loads Estimation

Unlike the lateral sides, the top and the bottom sides of each cabin compartment consist of multiple layers of shell and insulation materials. Both at the top and at the bottom, the sequence of layers from the outside of the cabin to the inside is as follows: CMC (shell, L1), glass fiber (insulation material, L2), boil-off hydrogen/air (insulation material), and glass fiber (insulation material, L3). Thicknesses and conductivities of the layers' materials of the cabin compartment are reported in Table 3. Through the layers of CMC and glass fiber conductive heat transfer occurs, whereas through either the layer of boiled-off hydrogen or air convective heat transfer happens, where

the fluid flows inside the duct and absorbs a portion of the incoming heat load. The insulation layer of boiled-off hydrogen is an alternative solution to the insulation layer of air [26]. Six thickness values were investigated for the layer of boiled-off hydrogen, whereas only two (i.e., 40 and 60 mm) were considered for the layer of air. The higher convective heat exchange guaranteed by the boiled-off hydrogen should be traded-off against the most critical materials compatibility and integration issues of hydrogen with respect to air.

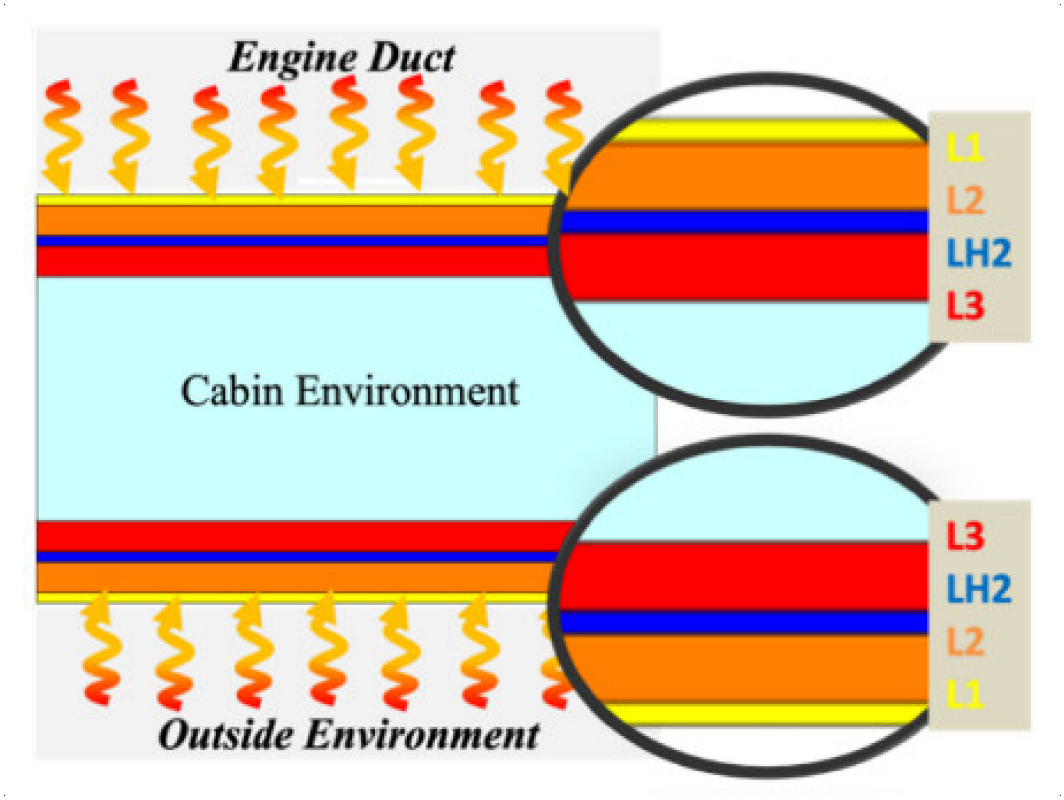

Figure 14. Cross-section of the cabin compartment.

Knowing the temperature of the external bottom skin of the cabin (wall temperature), the temperature of the upper external skin of the cabin (engine duct temperature), the additional thermal power provided by the onboard systems, the thermal conductivities, the thicknesses and surfaces of the materials' layers, and considering as a constraint that the internal temperature of the cabin can vary between 18 and 25 °C, the heat loads acting on the bottom and on the top of the cabin only through conductive transfer were computed, respectively, using Equations (15) and (16) by exploiting the electrical analogy (see also Equation (17)).

$$(\dot{Q}_{cab\ bottom})_{cond} = \frac{T_w - T_{int}}{R_{inf}} \tag{15}$$

$$(\dot{Q}_{cab\ top})_{cond} = \left[(\dot{Q}_{cab\ top})_{cond}\right]_{eng} + \left[(\dot{Q}_{cab\ top})_{cond}\right]_{subsys} = \left(\frac{T_{eng} - T_{int}}{R_{sup}}\right) + \left[(\dot{Q}_{cab\ top})_{cond}\right]_{subsys} \tag{16}$$

$$R_{sup/inf} = \frac{t_{L1}}{k_1 S_{sup/inf}} + \frac{t_{L2}}{k_2 S_{sup/inf}} + \frac{t_{L3}}{k_3 S_{sup/inf}} + \frac{1}{h_a S_{sup/inf}} \tag{17}$$

Table 3. Thicknesses and conductivities of the layers' materials of the cabin compartment.

Layer		Material	Thick (mm)	k (W/m/K)
Shell	L1	CMC		15
Insulation	L2	Glass fiber	50	0.1
	L3			(-)
	LH_2	Boil-off H_2	0.5 1 1.5 2.0 2.5 3.0	

The contribution of the insulation layer of boiled-off hydrogen to the estimation of the heat load was modeled as convective heat transfer, considering it as a fluid that flows inside a duct with a constant surface heat flow. The heat absorbed by boiled-off hydrogen through the hydrogen insulation layer was calculated using Equations (18) and (19):

$$(\dot{Q}_{cab\ bottom})_{conv} = (\dot{Q}_{cab\ top})_{conv} = -\dot{m}_{H2} c_{p\mathrm{H2}} \Delta T_{H2}, \tag{18}$$

$$\dot{m}_{H2} = \rho_{H2} w_{H2} A_{H2}, \tag{19}$$

Eventually, the heat loads acting on the bottom and on the top of the cabin through conductive and convective heat transfers are given, respectively, by Equations (20) and (21).

$$\dot{Q}_{cab_{bottom}} = (\dot{Q}_{cab\ bottom})_{cond} + (\dot{Q}_{cab\ bottom})_{conv} = \frac{T_w - T_{int}}{R_{inf}} - \dot{m}_{H2} c_{p\mathrm{H2}} \Delta T_{H2} \tag{20}$$

$$\dot{Q}_{cab_{top}} = (\dot{Q}_{cab\ top})_{cond} + (\dot{Q}_{cab\ top})_{conv} = \frac{T_{eng} - T_{int}}{R_{sup}} + \left[(\dot{Q}_{cab\ top})_{cond}\right]_{subsys} - \dot{m}_{H2} c_{p\mathrm{H2}} \Delta T_{H2} \tag{21}$$

The boiled-off hydrogen density was hypothesized to be equal to $\rho_{H2} = 0.33\ \mathrm{kg/m^3}$, its speed inside the duct ranged between $w_{H2} = 70\ \mathrm{m/s}$ and $w = 100\ \mathrm{m/s}$, and the variation of boiled-off hydrogen temperature inside the duct was assumed to be equal to $\Delta T_{H2} = 15\ \mathrm{K}$.

3.2.5. ECS Performance

Once the total heat loads acting on the cabin were computed, the air mass flow, m, that the ECS should provide could be calculated by Equation (2).

Considering that the selected worst-case scenario was the hot case when the vehicle flies at hypersonic speed from Mach 4 to Mach 8 and that the architecture of the ECS was bleed-less, the input values of the temperature and pressure of the air entering the CAU were theoretically those of the ram-air at the inlet combustor ahead of the struts. However, the pressure of the ram-air extracted by the engine inlet duct may still be too low to comply with the requirements at the CAU's exit of 253 K for the air temperature and 8×10^4 Pa (0.8 bar) for the air pressure. In this case, a dedicated auxiliary compressor was integrated ahead of the primary heat exchanger. The ram-air extracted by the engine inlet duct entered first the dedicated auxiliary compressor and then flowed through the CAU (Figure 9) to finally exit it. By imposing the required output values of air temperature and pressure and knowing the input values of air temperature and pressure in different flight conditions, it was possible to obtain the power supplied by the turbine and the necessary mass flow rate of the refrigerant fluid (boiled-off hydrogen) for the heat exchangers.

To mathematically model the CAU, the air was considered as an ideal gas with the following properties: (i) point molecules with negligible volume; (ii) only elastic collisions; (iii) non-interacting molecules.

Knowing the temperature of the air at the exit of the turbine, the inlet temperature was calculated as follows:

$$T_3 = \frac{T_4}{1 - \eta_t \left(1 - \left(\frac{1}{\beta_t}\right)^{\frac{\gamma-1}{\gamma}}\right)} \tag{22}$$

The turbine efficiency, η_t, was set equal to 0.9, while the turbine expansion ration, β_t, was 6 [28]. Knowing the pressure of the air at the exit of the turbine, the inlet pressure was calculated as follows:

$$P_3 = P_4 \cdot \left(\frac{T_3}{T_4}\right)^{\frac{\gamma}{\gamma-1}} \tag{23}$$

The power supplied by the CAU's turbine could thus be computed:

$$P_t = \eta_{mt} \dot{m} c_p (T_3 - T_4) \tag{24}$$

The mechanical efficiency of the turbine, η_{mt}, was set equal to 0.9 [28].

The temperature of the air at the turbine inlet has the same value at the heat exchanger's exit. The temperature of the air entering the heat exchanger, T_2, is obtained by assuming a mass flow rate of the coolant mean (boiled-off hydrogen) equal to 10% [24] of the air mass flow:

$$T_2 = T_3 + \frac{\dot{m}_{H2II} c_{pH2} (T_{outH2II} - T_{inH2II})}{\dot{m} c_p} \tag{25}$$

The specific heat capacity of boiled-off hydrogen, c_{pH2}, has been assumed equal to 11,720 $\frac{\mathrm{J}}{\mathrm{kgK}}$, while the temperature of the boiled-off hydrogen entering the heat exchanger, T_{inH2II}, has been hypothesized equal to 30 K and that one exiting the heat exchanger, $T_{outH2II}$, equal to 100 K.

The pressure of the air entering the heat exchanger in the same section is obtained by assuming a typical value of 3% of leakage6 to estimate the pressure drop of the air through the heat exchanger:

$$P_2 = \frac{P_3}{0.97} \tag{26}$$

The temperature of the air entering the secondary heat exchanger is the same as the temperature of the air exiting the compressor. The temperature of the air entering the CAU's compressor can thus be computed as follows:

$$T_1 = \frac{T_2}{1 + \frac{1}{\eta_c}\left(\beta_c^{\frac{\gamma-1}{\gamma}} - 1\right)} \tag{27}$$

The compressor efficiency, η_c, has been set equal to 0.85. The pressure of the air entering the compressor is expressed by Equation (28):

$$P_c = \eta_{mc} \dot{m} c_p (T_2 - T_1) \tag{28}$$

The power required by the CAU's compressor can thus be computed:

$$\dot{m}_{H2I} = \frac{\dot{m} c_p (T_0 - T_1)}{c_{pH2}\left(T_{outH2_I} - T_{inH2_I}\right)} \tag{29}$$

Knowing the temperature of the air at the auxiliary compressor inlet, T_0, i.e., the temperature of the ram-air extracted from the engine air inlet, and the temperature of the air entering the CAU, the mass flow of the boiled-off hydrogen, as coolant mean of the first exchanger of the CAU, is calculated as follows:

$$\dot{q}_{external} = h_{conv}(T_{rec} - T_w) \tag{30}$$

The temperatures of the boil-off hydrogen entering and exiting the primary heat exchanger were hypothesized to be equal to the values of the secondary heat exchanger.

Knowing the flight conditions and the overall vehicle layout, the process starts from the definition of the cabin requirements in terms of temperature and minimum air mass flow. Subsequently, the temperature of the external wall of the aircraft is determined by means of convective–radiative–conductive heat transfer balance. Then, once the geometric dimensions of the cabin are known, intrinsic properties, such as thicknesses and thermal conductivities, are hypothesized. This allows to determine the incoming heat flux and the subtractive heat flux due to the convective insulation layer. Consequently, the air mass flow that the ECS should supply to meet the requirements is calculated. In the case the air mass flow is lower than the minimum value prescribed by CS-25, it is necessary to recalculate it by modifying the convective insulation layer' thickness. Otherwise, knowing the required air mass flow, the power demand of the CAU can be estimated. The air temperature and pressure conditions at the exit of the turbine of the CAU are known, as well as the input values of the ram-air extracted by the engine inlet duct. The process to size the power to drive the compressor and the power available at the turbine can thus be completed. If the estimated air pressure entering the CAU, P_1, is lower than that the pressure of the ram-air extracted by the engine inlet duct, P_0, an auxiliary compressor is required.

4. Application to the Case Study and Discussion of the Results

The equilibrium equation (Equation (4)) was solved, and the wall temperature was plotted as a function of Mach number for three different emissivity values (Figure 15). If ceramic matrix composite materials (ε = 0.8) were considered, the wall temperature remained below 1300 K for all Mach numbers.

The wall temperature and the recovery temperature for each Mach number of the hypersonic field are reported in Table 4.

The heat loads acting on or inside the cabin (external heat load acting on the external skin, internal heat load generated inside the cabin, and internal heat load acting on the external skin of the cabin) are shown in Figure 16. External heat loads acting on the external skin of the cabin ("deck side" in the legend of Figure 16) increased with the Mach number as the wall temperature increased. Internal heat loads acting on the external skin of the cabin due to the propulsive compartment ("engine" in the legend of Figure 16) increased as well with the Mach number. Conversely, the contribution to the internal heat loads acting on the external skin of the cabin due to the onboard systems and internal heat loads generated inside the cabin did not depend on the Mach number.

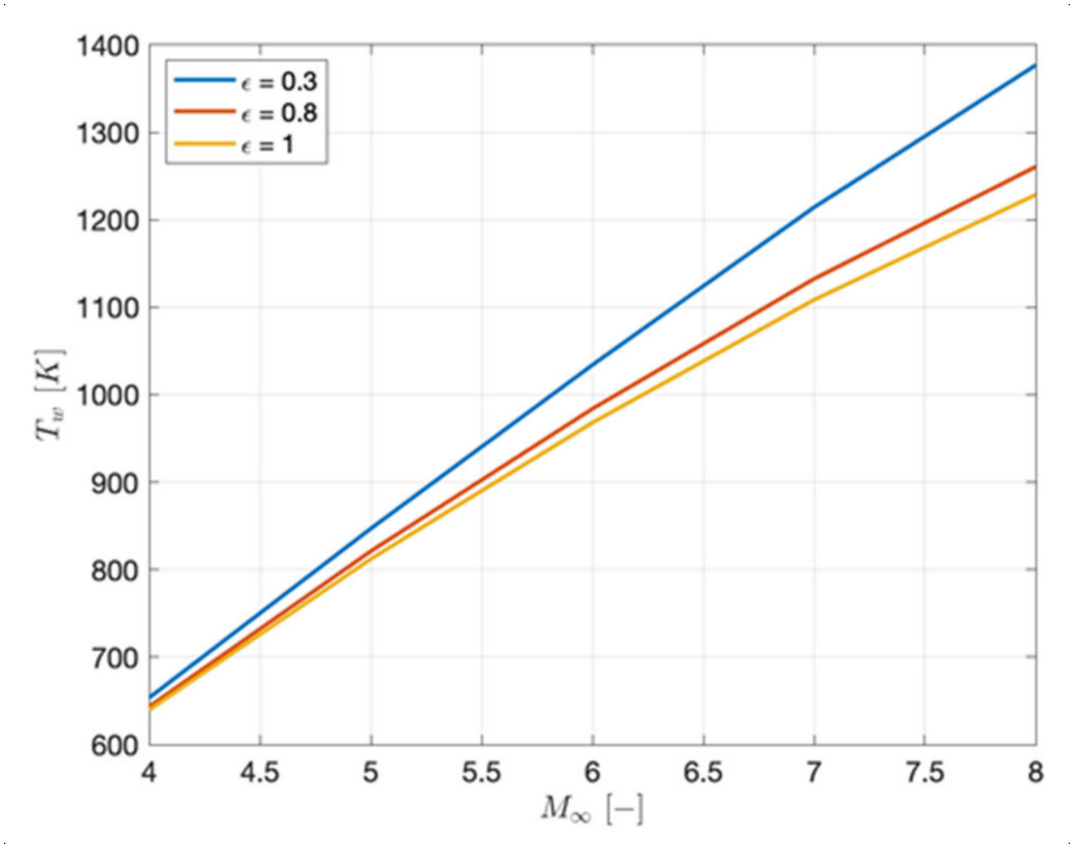

Figure 15. Wall temperature as function of the Mach number for different emissivity values.

Table 4. Recovery temperature and wall temperature for different Mach numbers.

Mach	4	5	6	7	8
T_{rec} (K)	625.03	819.91	1019.29	1226.22	1429.86
T_{wall} (K) for $\epsilon = 0.8$	643.34	821.13	984	1132.60	1260.72

Figure 17 depicts the variation of the heat loads with the Mach number and cabin compartments. Heat loads were here calculated for the fixed values of thickness and speed of the boil-off hydrogen insulation layer. Specifically, the thickness of 2 mm and the speed of 70 m/s were considered (Figures 16 and 17). Total heat loads were higher for compartment number two and compartment number three, if compared to the other cabin compartments, because the surfaces at the top and the bottom of compartments two and three were bigger, thus leading to higher external heat loads (Equation (15)) and internal heat loads acting on the external skin of the cabin (Equation (16)). In addition, compartment number two and compartment number three had the highest number of passengers with respect to the remaining cabin compartments, thus implying also higher internal heat loads.

Sensitivity analyses were performed to understand the impact of the fluid of the convective insulation layer (boil-off hydrogen and air) and the thickness and the speed of the convective insulation layer onto the heat loads.

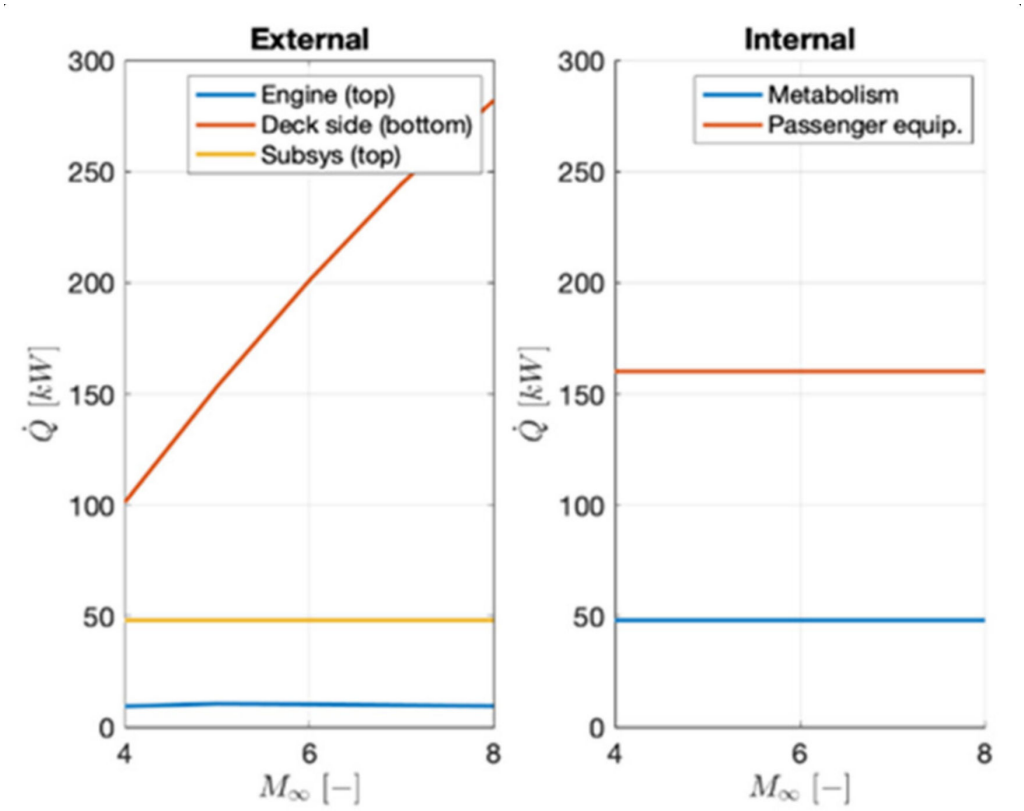

Figure 16. Variation of different types of heat loads for the aircraft with the Mach number for the fixed values of thickness and speed of the boil-off hydrogen insulation layer.

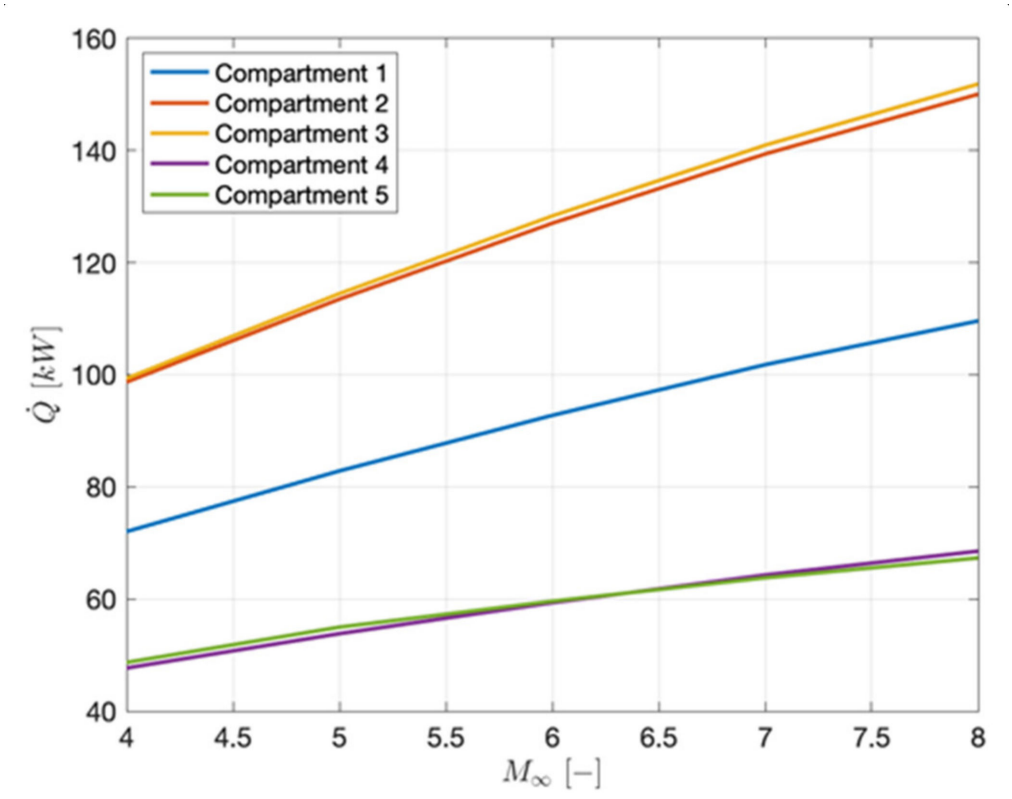

Figure 17. Variation of total heat load with the Mach number per each compartment for fixed values of thickness and speed of the boil-off hydrogen insulation layer.

Figure 18a,b depict, respectively, the variation of total heat loads with the thickness of boil-off hydrogen insulation layer for the different cabin compartments at Mach 4 and at Mach 8 flight conditions. The results reveal that total heat loads were generally higher for compartments number two and number three of the cabin as previously highlighted (Figure 17). However, the impact of the thickness of the hydrogen boil-off insulation layer was significant: the bigger the thickness of the hydrogen insulation layer, the lower the total heat loads, but the correlation was not the same for all cabin compartments with the curves for compartments number two and number three being steeper than those of the remaining compartments because of their bigger exchange surfaces. This lead to the lowest values of total heat loads for compartments number two and number three, if compared to the other cabin compartments, for thicknesses of the hydrogen layer above 2 mm at low hypersonic speeds. It is worth remembering that the high dependency of the heat loads on the thickness of the hydrogen layer was only due to the influence of thickness on the external heat load acting on the cabin and the internal heat load acting on the external skin of the cabin. In Figure 18a,b, the speed of boil-off hydrogen was considered fixed and equal to 70 m/s as a conservative hypothesis.

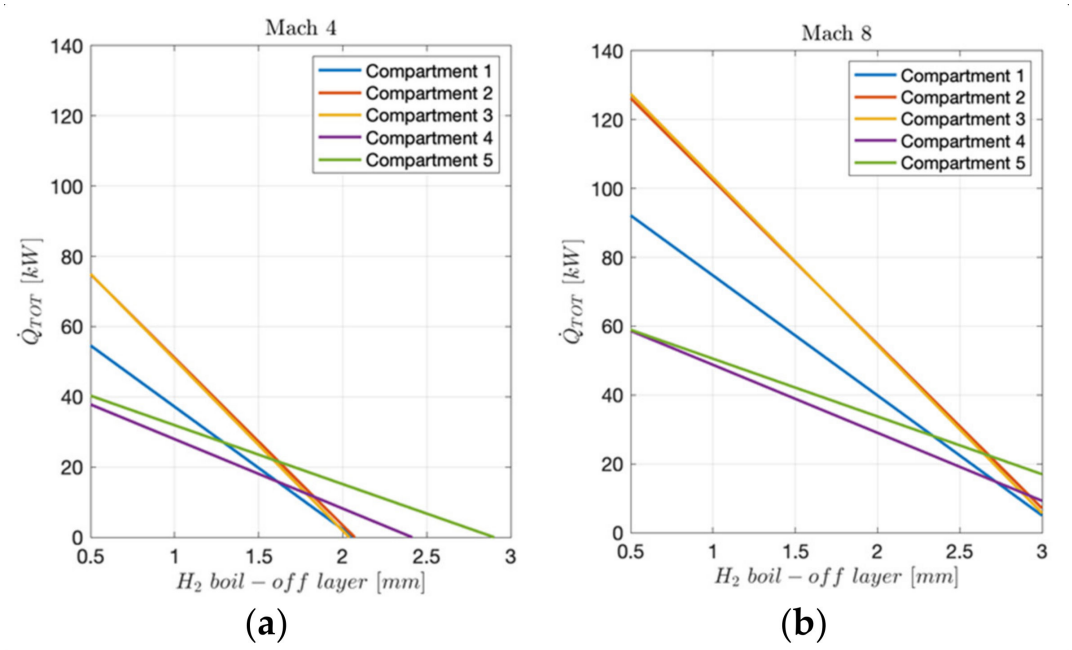

Figure 18. (**a**) Variation of the total heat loads with the thickness of the hydrogen boil-off insulation layer per each cabin compartment at Mach 4 flight condition; (**b**) variation of total heat loads with the thickness of the hydrogen boil-off insulation layer per each cabin compartment at Mach 8 flight condition.

Eventually, Figure 19a,b summarize the results of the sensitivity analysis on the thickness of the boil-off hydrogen convective layer, comparing the internal and external heat loads acting on the cabin with the subtractive heat loads provided by the boil-off hydrogen layer surrounding the cabin's inner wall.

It is worth remembering that the enhancement of the cooling performance due to the increase in the convective layer's thickness should be traded off against the increase in overall aircraft mass and, consequently, thrust requirements.

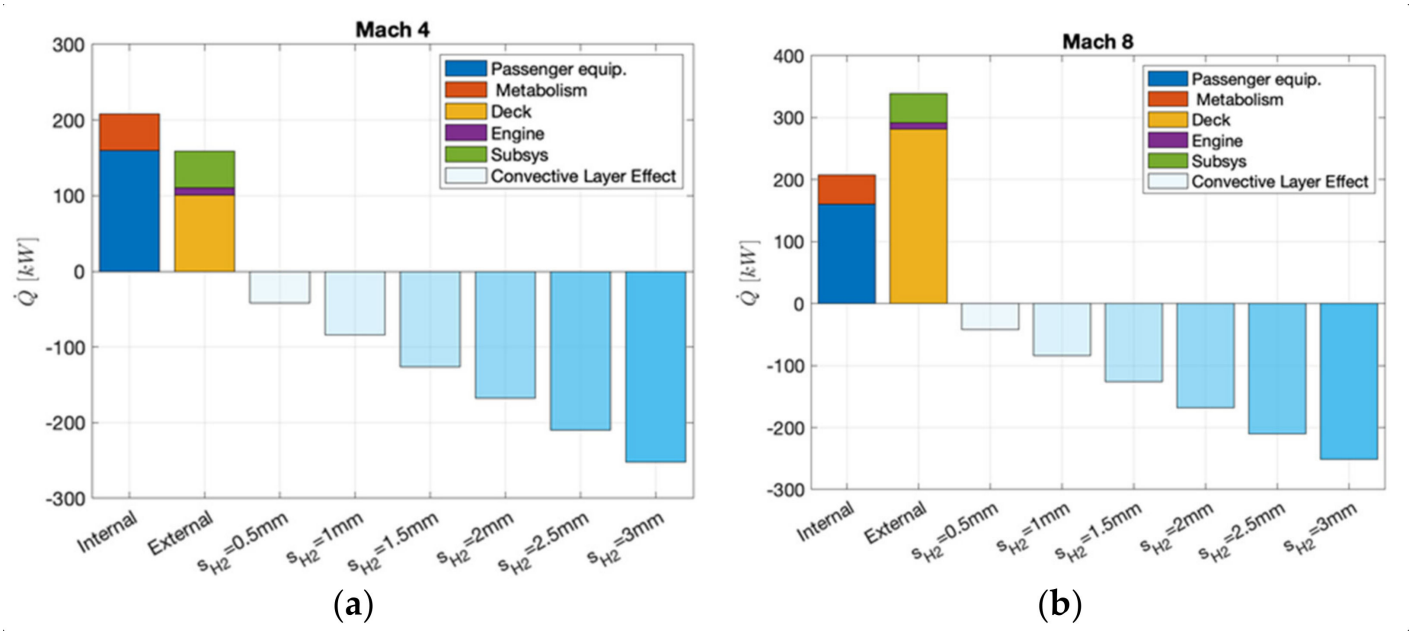

Figure 19. (**a**) Summary of the internal and external heat loads acting on the cabin and estimated air convective layer effect at Mach 4 flight conditions; (**b**) summary of the internal and external heat loads acting on the cabin and estimated air convective layer effect at Mach 8 flight conditions.

As anticipated, another solution, envisaging air as a fluid of the convective insulation layer was thoroughly analyzed, and the results compared those obtained with boil-off hydrogen. To properly select the thicknesses of the convective layer and the re-circulation speed of the air in the channel, the same mass flow of the fluid was considered (see Equation (31)):

$$\rho_{H2} w_{H2} A_{H2} = \rho_{air} w_{air} A_{air}, \tag{31}$$

where ρ_{H2} and ρ_{air} are, respectively, the density of the boil-off hydrogen and of the air in (kg/m^3), w_{H2} and w_{air} are their speeds (m/s), and A_{H2} and A_{air} are the cross-sectional areas of the convective channel. Considering that the area of the channel was schematically represented as a simple rectangular shape and assuming the same width of the cross-section (approximately the cabin compartment width), Equation (31) can be rewritten as follows:

$$\frac{w_{air} t_{air}}{w_{H2} t_{H2}} = \frac{\rho_{H2}}{\rho_{air}}, \tag{32}$$

An alternative solution to the convective insulation layer of boil-off hydrogen may thus be a 60 mm thick convective layer, filled with air re-circulating at 0.7 m/s, reaching a mass flow of 0.5 kg/s (i.e., the same mass flow value obtained with a 2 mm thick convective layer of boil-off hydrogen flowing at 70 m/s).

The results show that compartments number two and number three are always those that experience the highest heat loads both at low and high Mach numbers of the hypersonic speed regime, if compared to the other cabin compartments. However, the change of fluid for the convective insulation layer revealed that the impact of the thickness of the layer for the air was almost negligible onto the heat loads. In fact, while for the boil-off hydrogen insulation layer, an increase of 1 cm of thickness implied a decrease of approximately 100 kW of heat loads, thanks to the high efficiency of the fluid; for the air insulation layer, an increase of 10 cm of thickness allowed for a decrease of less than 5 kW of heat loads.

Figure 20a,b illustrate the sensitivity of the heat loads absorbed by the fluid (hydrogen boil-off in Figure 20a and air in Figure 20b) with respect to the thickness of the convective insulation layer and the speed of the fluid. The results show that, as already noticed for the overall heat loads, the effect of the insulation layer's thickness was significant on the heat loads absorbed by the boil-off hydrogen and negligible on the heat loads absorbed by the air. This is evident at low speeds of the fluid. As the speed values increased, the convective heat exchange guaranteed by the boil-off hydrogen layer and the air improved, but the general tendency was confirmed: an augment of 1 mm of thickness allowed for hundreds of kW of heat loads absorption for the hydrogen boil-off, while only for less than 5 kW for the air.

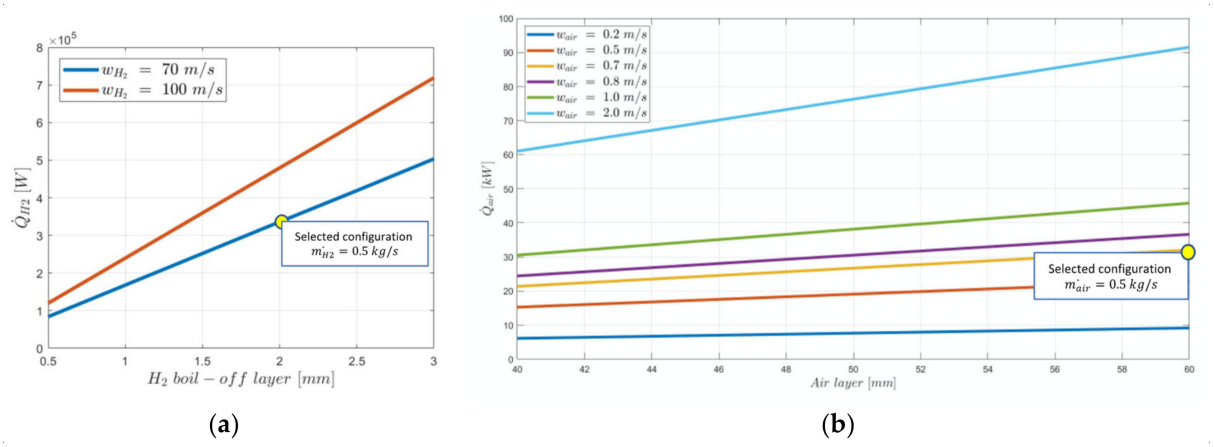

Figure 20. (**a**) Variation of heat loads absorbed by the boil-off hydrogen with the thickness of the insulation layer and different values of the speed of the fluid; (**b**) variation of heat loads absorbed by the air with the thickness of the insulation layer and different values for the speed of the fluid.

The air mass flow that the ECS should supply was computed using Equation (2). Figure 21a–c show the variation of the request of total air mass flow for the aircraft with Mach number, whereas Figure 22a–c depict the variation of the request of total air mass flow per cabin compartment with Mach number. Three values of thickness of the boil-off hydrogen insulation layer (i.e., 0.5, 2, and 3 mm) were selected and analyzed. The speed of the fluid was set equal to 70 m/s as a conservative hypothesis.

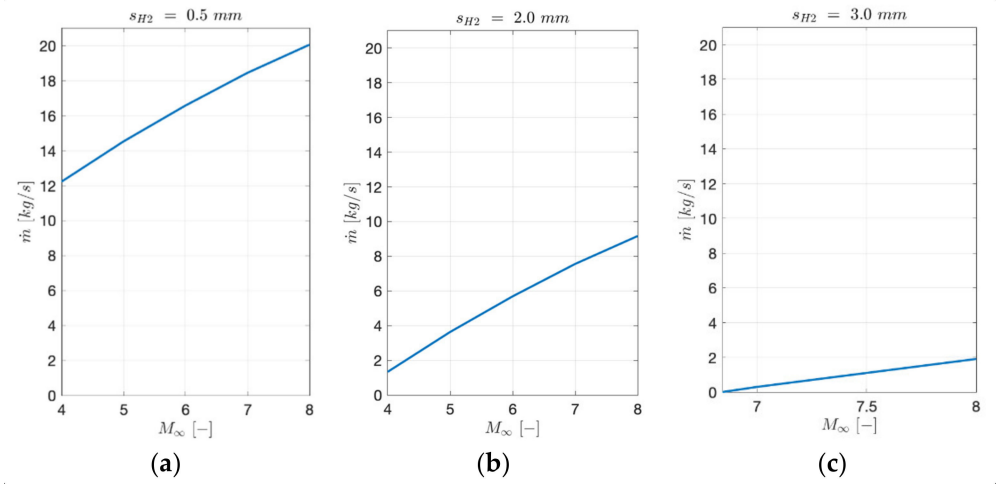

Figure 21. (**a**) Variation of the overall air mass flow supplied by the ECS with Mach number for the cabin (thickness of the boil-off hydrogen insulation layer equal to 0.5 mm); (**b**) variation of the overall air mass flow supplied by the ECS with Mach number for the cabin (thickness of the boil-off hydrogen insulation layer equal to 2 mm); (**c**) variation of the overall air mass flow supplied by the ECS with Mach number for the cabin (thickness of the boil-off hydrogen insulation layer equal to 3 mm).

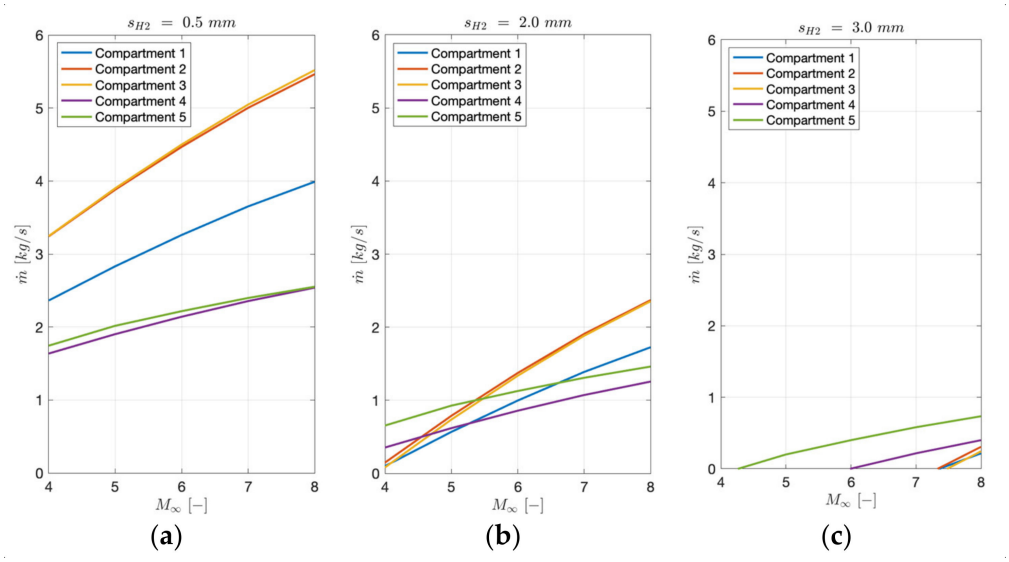

Figure 22. (**a**) Variation of the air mass flow supplied by the ECS with Mach number for each cabin compartment (thickness of the boil-off hydrogen insulation layer equal to 0.5 mm); (**b**) variation of the air mass flow supplied by the ECS with Mach number for each cabin compartment (thickness of the boil-off hydrogen insulation layer equal to 2 mm); (**c**) variation of the air mass flow supplied by the ECS with Mach number for each cabin compartment (thickness of the boil-off hydrogen insulation layer equal to 3 mm).

Figures 21 and 22 clearly show how the air mass flow rate required to cool down the cabin decreased as the thickness of the boil-off hydrogen insulation layer increased. As highlighted in Figure 18a, as the thickness of the boil-off hydrogen increased above 1.5 mm, the heat loads acting on compartments number two and number three were lower than those acting on the other cabin compartments for low Mach numbers, thanks to the bigger exchange surfaces of compartments number two and number three. Consequently, the air mass flow that the ECS should supply to cool down the cabin had the lowest value in this condition for compartments number two and number three.

It is worth noting that the air mass flow required was higher than the minimum quantity recommended by CS-25, that is $\dot{m} \geq 0.25$ kg/minper passenger. Typical air mass flow provided by ECS through the engine bleed for a wide body aircraft was 10–20 kg/s. These values are in line with those obtained with 2 mm of thickness of the boil-off hydrogen insulation layer, which can thus be selected as the thickness's value.

For comparisons, Figure 23 refers to A380 ECS air flow requirements for different mission phases [29].

Figure 24a,b show the variation with the Mach number of the air mass flow that the ECS should supply to the cabin and to the single compartments, in the case that the air is the fluid of the convective insulation layer. The results revealed that the air mass flow that should be provided by the ECS was higher than the typical values expected for a wide body subsonic aircraft, considering the maximum thickness of 60 mm for the insulation layer and a speed of 0.2 m/sec for the fluid.

Eventually, Figure 25a,b summarize the results of the sensitivity analysis on the thickness of the air convective insulation layer, comparing the internal and external heat loads acting on the cabin with the subtractive heat loads provided by the air layer surrounding the cabin inner wall. This has led to the conclusion that the boil-off hydrogen should be chosen as the preferable fluid for the convective insulation layer, both for its higher convective heat exchange performance and for the more compact cross-sectional configuration of the cabin, notwithstanding the issues of materials compatibility.

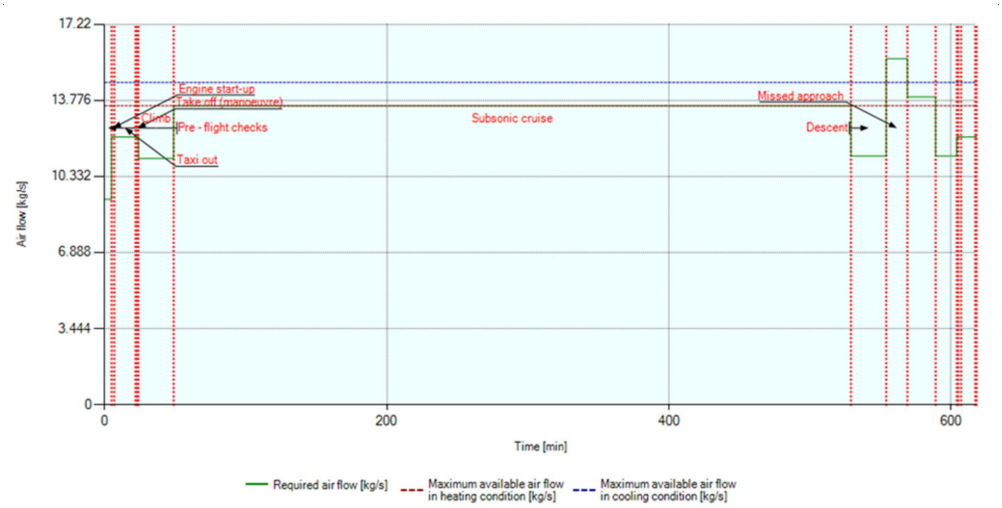

Figure 23. Estimation of air mass flow supplied by ECS through engine bleed and CAU for a wide body aircraft.

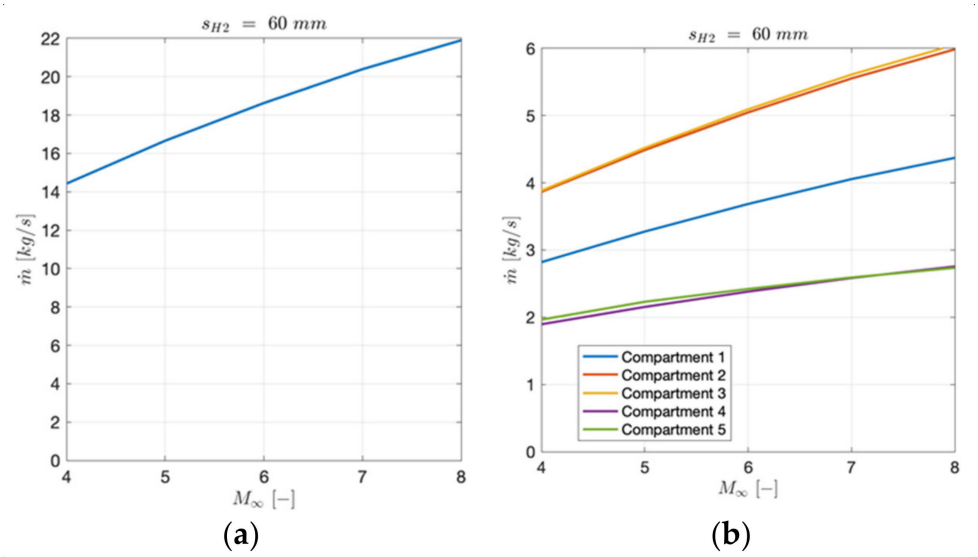

Figure 24. (**a**) Variation in the overall air mass flow supplied by the ECS with the Mach number for the aircraft (thickness of the air insulation layer equal to 60 mm); (**b**) variation in the air mass flow supplied by the ECS with the Mach number for each cabin compartment (thickness in the air insulation layer equal to 60 mm).

Knowing the required air mass flow, it is possible to estimate the available power from the CAU's turbine to drive the CAU's compressor. The pressure and temperature values of the ram-air extracted from the engine air inlet at pre-combustion conditions for Mach numbers ranging from 4 to 8 are reported Table 5. These values are inputs for the calculation of power supplied by the turbine.

Figures 26a,b and 27 show the variation in the power supplied by the turbine to drive the compressor of the CAU (available power vs. requested power) for different values of thickness of the boil-off hydrogen layer. The figures also highlight the impact of the expansion ratio of the turbine, which ranges between 2 and 5, and the compression ratio of the compressor, which ranges between 1.2 and 2.5, as typical values of a conventional aircraft's CAU. The results reveal that the turbine can drive the compressor throughout the hypersonic speed regime, i.e., the hot case and worst case scenarios, for all thicknesses of the hydrogen boil-off insulation layer of the cross-sectional configuration of the cabin. This implies that the open loop cycle with the air cycle machine is a feasible technical solution for all Mach numbers and all flight altitudes for the ECS.

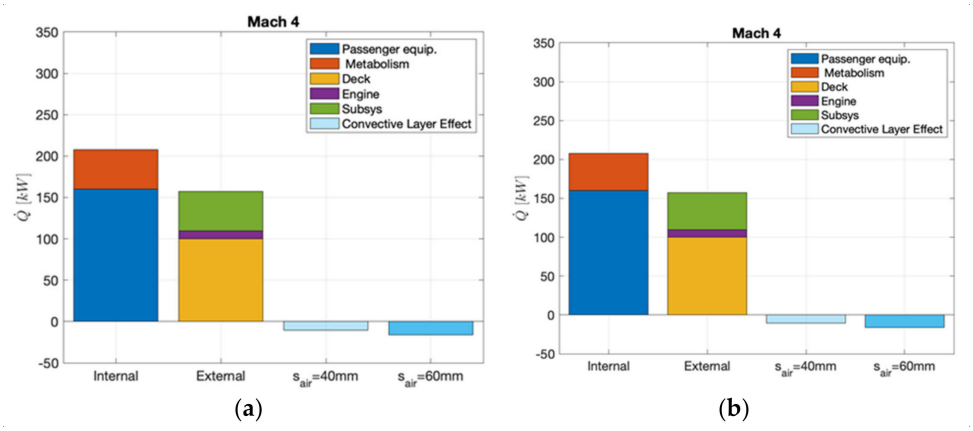

Figure 25. (**a**) Summary of internal and external heat loads acting on the cabin and estimated air convective insulation layer effect at Mach 4 flight condition; (**b**) summary of internal and external heat loads acting on the cabin and estimated air convective insulation layer effect at Mach 8 flight conditions.

Table 5. Pressure and temperature levels at pre-combustion conditions for different Mach numbers.

Mach	4	5	6	7	8
$P_{air\ pre\text{-}comb}$ (Pa)	70,756.32	59,669.83	40,073.57	31,095.77	26,610.29
$T_{air\ pre\text{-}comb}$ (K)	547.15	573.40	621.63	674.24	734.0

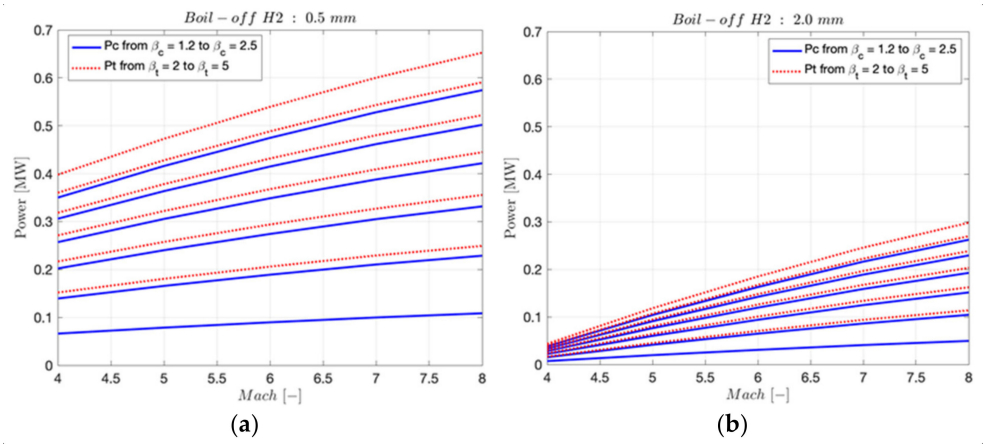

Figure 26. (**a**) Variation of the available (turbine) vs. required (compressor) power of the CAU with Mach number for a 0.5 mm thick boil-off hydrogen insulation layer; (**b**) variation of the available (turbine) vs. required (compressor) power of the CAU with Mach number for 2 mm thick boil-off hydrogen insulation layer.

It is worth noting that the bigger the thickness of the insulation layer, the lower the requested power to drive the compressor of the CAU. The excess of power can be used to supply additional loads, for example, the fan to recirculate air from the cabin to mix it with the air exiting the CAU.

Figure 27b illustrates the variation of the compression ratio of the dedicated auxiliary compressor as a function of the Mach number for different values of the compression ratio of the CAU's compressor, which ranged from 1.20 to 2.50. It clearly emerges that as the flight speed and altitude increased, it was necessary to compress more the incoming air to meet the performance requirements at the CAU's exit. In addition, the higher the compression ratio of the CAU's compressor, the lower the values of the compression ratio of the auxiliary compressor. It is worth noting that the auxiliary compressor should be able to vary its compression ratio with the flight's Mach number.

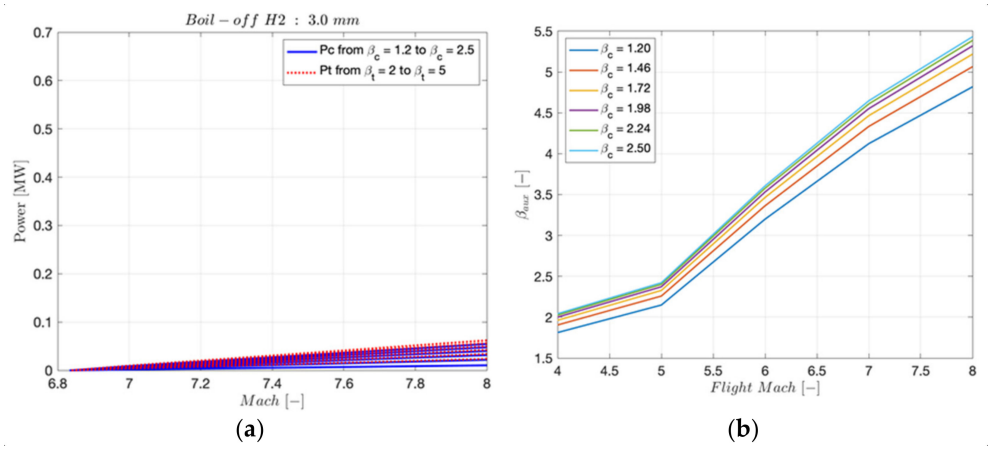

Figure 27. (**a**) Variation of the available (turbine) vs. required (compressor) power of the CAU with Mach number for 3 mm thick boil-off hydrogen insulation layer; (**b**) variation of the compression ratio of the auxiliary compressor with the Mach number for different values of the compression ratio of the CAU's compressor.

Considering as a hypothesis the compression ratio of the CAU's compressor to be equal to $\beta_c = 1.9$, the variation of the required power to drive the auxiliary compressor as function of the Mach number was plotted in Figure 28a for different values of thickness of the boil-off hydrogen insulation layer. The results show that the thicker the boil-off hydrogen layer, the lower the required power to drive the auxiliary compressor. Alternatively, different locations for the ram-air extraction by the engine inlet can be investigated. Higher pressure values of the ram-air should be traded off against detrimental effects on engine performance.

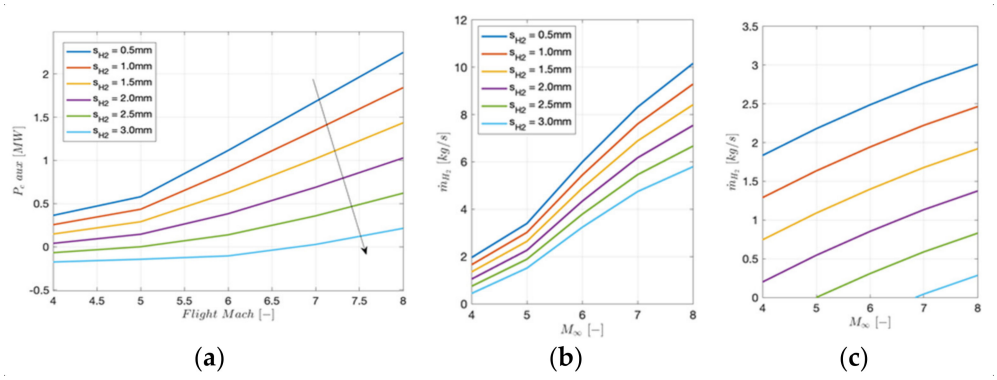

Figure 28. (**a**) Auxiliary compressor power (required power) as function of the Mach number for different values of thickness of the boil-off hydrogen insulation layer; (**b**) variation of the boil-off hydrogen mass flow of the primary heat exchanger with the Mach number for different thicknesses of the insulation layer; (**c**) variation of the boil-off mass hydrogen mass flow of the secondary heat exchanger with the Mach number for different thicknesses of the insulation layer (see legend in Figure 28b).

The mass flow rate of the boil-off hydrogen as coolant mean of the primary heat exchanger of the CAU is plotted in Figure 28b as function of the Mach number, ranging from Mach 4 to Mach 8, for different values of thickness of the boil-off hydrogen convective insulation layer of the cabin cross-section. The results revealed that the higher the thickness of the hydrogen layer, the lower the boil-off hydrogen mass flow required by the primary heat exchanger. The same considerations hold true for the variation of the boil-off hydrogen mass flow of the secondary heat exchanger with the Mach number and thickness of the hydrogen layer of the cabin cross-section as depicted in Figure 28c. The hypothesis that the mass flow of the boil-off hydrogen can be estimated as 10% of the air mass flow supplied by the ECS was verified by the performance assessment of the multi-functional TEMS, where here made to estimate the mass flow of the boil-off hydrogen as coolant mean.

5. Conclusions

Conclusions can be summarized as follows:

1. The design and performance assessment of an innovative environmental control system for future hypersonic civil aircraft propelled by cryogenic liquid hydrogen was developed. The ECS was integrated within the complex multi-functional thermal and energy management system that managed the heat loads and the generation of electric power through the exploitation of hydrogen, both as liquid and as boil-off. The use of hydrogen pushes the concept of onboard systems integration further, which is key for high-speed vehicles' success and guarantees the decarbonization of flights. Moreover, boil-off hydrogen can be used to cool down the aeroshell that is heated up at high speeds, thus exploiting the liquid hydrogen not only as coolant means but as heat rejection and, therefore, allowing the recovery of part of the viscous power dissipation by returning this energy back into the engine;
2. Cold case and hot case scenarios of hypersonic aircraft were significantly different from the cold case and hot case scenarios of the subsonic aircraft. For hypersonic aircraft, the cold case scenario occurred either when parking on ground in the engine-off mode of operation without passengers onboard, or in the subsonic climb/cruise phases at 5000–10,000 m of altitude without passengers; the hot case scenario occurred in cruise phase at the highest Mach number in the engine-on mode of operation with passengers at full capacity;
3. Unlike subsonic aircraft, the heat loads budget for hypersonic aircraft should consider additional internal heat loads generated outside the cabin's external skin but inside the vehicle itself: they are mainly due to the propulsive system embedded in the vehicle because of the highly integrated configuration of the hypersonic vehicle;
4. The results of in-depth analyses of integrated onboard systems' sizing for hypersonic aircraft confirm the rule of thumb for space systems that equals the order of magnitude of aircraft mass budget in tons to the order of magnitude of the aircraft power budget in kW. Unlike traditional subsonic aircraft architecture, the request of electric power for cabin avionic systems of future high-speed or low-speed civil passenger windowless aircraft will significantly increase. Consequently, the heat loads generated inside the cabin will rise. The estimation of the internal heat loads for high-speed civil aircraft cannot be based on statistical relationships of traditional subsonic aircraft. For this purpose, analytical formulations based on calculations of electric power demands are developed;
5. Detailed thermal analyses were carried out to properly assess the temperature distributions and the thermal power along the entire length of the inner compartments of the vehicle due to the presence of the air-breathing engines, which for hypersonic vehicles generally extend from the front up to the rear part of the aircraft. The results reveal that the highest temperatures (up to 300 °C) were reached when the aircraft was slowing down during the descent phase because of the heat load accumulated during the entire trajectory. Therefore, the end of the cruise condition could be considered the worst-case scenario (hot case) for hypersonic cruisers;
6. Comparisons between high-fidelity simulations for thermal analysis including or not the modeling of cryogenic tanks and their internal temperature evolution along the mission show the beneficial effect of distributed cryogenic hydrogen tanks onboard the aircraft on temperatures and, consequently, heat fluxes on external cabin compartments. It is possible to assert that the massive presence of cryogenic propellant onboard can contribute to lower the temperatures inside the vehicle and, consequently, heat fluxes entering the cabin up to 70%;
7. On the basis of the results of the detailed thermal analyses, the estimation of the heat loads generated inside the vehicle by the onboard systems integrated outside the passenger cabin were reviewed. Unlike traditional subsonic civil aircraft, the heat loads generated by onboard systems inside hypersonic aircraft (but outside cabin compartments), propelled by cryogenic hydrogen, can be estimated to be equal to 30%

of the electric power demand of the onboard systems themselves, assuming that the distributed integration of cryogenic tanks onboard the aircraft can lead to a reduction of up to 70% of temperatures and heat fluxes;

8. An innovative configuration of the cabin cross-section, which includes conductive and boil-off hydrogen convective insulation layers, was designed. The boil-off hydrogen is the cold source for both the heat exchangers of the cold air unit of the ECS and the convective insulation layer of the cabin compartments. The exploitation of the boil-off hydrogen allows for improving the cooling performance of the ECS in the hot case scenario (the worst case) without increasing the request of air mass flow, thus satisfying passengers' comfort requirements;
9. Comparisons between boil-off hydrogen and air as fluid of the convective insulation layer of the cabin cross-section configuration were analyzed in-depth and sensitivity analyses were performed, considering the thickness of the convective insulation layer and the speed of the fluid as parameters. The thickness of the insulation layer had a significant impact on the heat load absorption capability of the boil-off hydrogen, whereas it has a negligible impact on the air: an increase of 1 mm of thickness allowed for hundreds of kW of heat load absorption for the boil-off hydrogen, while only less than 5 kW for air;
10. A boil-off hydrogen convective insulation layer of 2 mm of thickness for the cabin cross-sectional configuration was selected as the most efficient one for long-range hypersonic aircraft, keeping the air mass flow supplied by ECS comparable to the typical values expected for wide body subsonic aircraft. The boil-off hydrogen should thus be chosen as the preferable fluid for the convective insulation layer both for its higher convective heat exchange performance and for the more compact cross-sectional configuration of the cabin, notwithstanding the issues of materials compatibility;
11. The open loop cycle with the air cycle machine for the CAU is a feasible technical solution for all Mach numbers and all flight altitudes for the ECS of hypersonic cruiser, considering the boil-off hydrogen convective insulation layer as the inner layer of the cabin cross-section, as testified to by the available power of the turbine of the CAU, which is able to drive the CAU's compressor throughout the flight (from ground up to stratospheric altitudes at Mach 8);
12. The environment control system architecture here disclosed is a clear example of the high-level of integration that characterizes high-speed vehicles at the subsystem level. To pursue a complete integration of the subsystems design and sizing into a wider aircraft design activity, model-based object-oriented systems engineering methodologies can be adopted as suggested in [30,31];
13. Future research activities will focus on the investigation of the capability of hydrogen to act as a key element of integration for onboard systems for space transportation products, ranging from suborbital vehicles [32] to reusable access to space and space tugs [33].

Author Contributions: Conceptualization, N.V. and R.F.; methodology, N.V., D.F. and R.F.; software, D.F. and R.S.; validation, D.F. and R.S.; formal analysis, N.V. and D.F.; writing—original draft preparation, R.F.; writing—review and editing, N.V.; visualization, D.F.; supervision, N.V.; funding acquisition, N.V. All authors have read and agreed to the published version of the manuscript.

Funding: This research was funded by European Union's Horizon 2020 research and innovation programme under grant agreement No. 769246 within the Stratospheric Flying Opportunities for High-Speed Propulsion Concepts (STRATOFLY) Project.

Acknowledgments: The authors would like to thank Luca De Giorgi for the valuable support provided during the post-graduate scholarship.

Conflicts of Interest: The authors declare no conflict of interest.

Nomenclature

A_{H2}	cross-sectional area of the hydrogen boil-off insulation layer (m^2)
A_{air}	cross-sectional area of the air insulation layer (m^2)
β_c	compressor's compression ratio
β_{aux}	auxiliary compressor's compression ratio
β_t	turbine's expansion ratio
c_p	air specific heat capacity (J/(kg*K))
c_{pH2}	hydrogen boil-off specific heat capacity at constant pressure (J/(kg*K))
c_f	turbolent skin friction coefficient
ΔT_{H2}	hydrogen boil-off temperature increase inside the duct (K)
γ	ratio of specific heat at a constant pressure and constant volume (i.e., 1.4)
ε	emissivity
h	altitude (m)
h_a	cabin air convective heat transfer coefficient ($W/(m^2K)$)
h_{conv}	convective heat exchange factor ($W/(m^2K)$)
k	thermal conductivity ($W/(mK)$)
K_{eq}	mode of operation coefficient
$\dot{m}$	air mass flow entering the cabin (kg/s)
$\dot{m}_{air}$	air mass flow in the convective insulation layer (kg/s)
$\dot{m}_{air\ intake}$	air mass flow extracted from the air intake (kg/s)
$\dot{m}_{bp}$	air mass flow of the by-pass line (kg/s)
$\dot{m}_{CAU}$	air mass flow entering the CAU (kg/s)
$\dot{m}_{engine\ bleed}$	air mass flow extracted from the engine (kg/s)
$\dot{m}_{H2}$	hydrogen boil-off mass flow in the convective insulation layer (kg/s)
$\dot{m}_{H2I}$	primary heat exchanger hydrogen boil-off mass flow (kg/s)
$\dot{m}_{H2II}$	secondary heat exchanger hydrogen boil-off mass flow (kg/s)
$\dot{m}_{ric}$	air mass flow recirculated from the cabin (kg/s)
M	Mach number
M_∞	free stream Mach number
$p_{air\_pre\text{-}comb}$	pressure of the air at pre-combustion condition (Pa)
$\dot{Q}$	total heat load (W)
n_{pax}	number of passengers
n_{crew}	number of crew member
μ_∞	free stream air viscosity (kg/(m·s))
ρ_∞	air density in standard condition (kg/m^3)
ρ_{H2}	hydrogen boil-off density (kg/m^3)
P_0	pressure of the ram-air extracted by the engine inlet duct (Pa)
P_1	pressure of the air at the compressor's inlet (Pa)
P_2	pressure of the air at the heat exchanger's inlet (Pa)
P_3	pressure of the air at the turbine's inlet (Pa)
P_4	pressure of the air at the exit of the turbine (Pa)
P_c	power required by the CAU's compressor (W)
P_t	power supplied by the CAU's turbine (W)
Pr	Prandtl number
R	recovery factor
Re_x	Reynolds number at a specific longitudinal location
σ	Boltzmann constant ($5.67 \cdot 10^{-8}\ \frac{W}{m^2K^4}$)
$S_{sup/inf}$	exchange surface between layers of the cabin cross-section (m^2)
S_t	Stanton number
t	skin thickness (m)
t_L	cabin cross-section conductive layer thickness (m)
t_{H2}	thickness of the convective hydrogen boil-off insulation layer (m)
t_{air}	thickness of the convective air insulation layer (m)
T_0	temperature of the ram-air extracted the engine inlet and entering the CAU (K)
T_1	temperature of the air at the compressor's inlet (K)
T_2	temperature of the air at the secondary heat exchanger's inlet (K)
T_3	temperature of the air at the turbine's inlet (K)
T_4	temperature of the air at the exit of the turbine (K)
T_{eng}	is the temperature of the upper side of the cabin, attached to engine duct (K)
T_{LH2}	LH_2 temperature (K)
T_{outH2I}	temperature of the hydrogen boil-off at the primary heat exchanger's exit (K)

$\dot{Q}_{external}$	external heat load acting on the external skin (W)
$\dot{Q}_{external\_cab}$	internal heat load acting on the external skin of the cabin (W)
$\dot{Q}_{external\_cab\_conductive}$	internal heat load acting on the external skin of the cabin only through conductive heat transfer (W)
$\dot{Q}_{tot}$	total heat load (W)
$\dot{Q}_{met}$	heat load due to metabolism (human beings) (W)
$\dot{Q}_{rest}$	heat load generated by metabolism at rest (W)
$\dot{Q}_{work}$	heat load generated by metabolism at work (W)
$\dot{Q}_{sysint}$	heat load due to onboard systems (W)
$\dot{Q}_{pax\_eq}$	electric power demand of the avionic equipment inside the cabin, related to passengers' comfort (W)
$(\dot{Q}_{cab\ top})_{cond}$	heat loads which are generated inside the vehicle but acting on the external skin of the cabin (W)
$\left[(\dot{Q}_{cab\ top})_{cond}\right]_{eng}$	heat loads coming from the engine compartment (W)
$\left[(\dot{Q}_{cab\ top})_{cond}\right]_{subsys}$	heat loads generated by all subsystems installed on the aircraft, but externally to the cabin (W)
$(\dot{Q}_{cab\ bottom})_{cond}$	heat loads acting on the lower side of the vehicle skin (W)
μ_{ref}	reference air viscosity (kg/(m·s))
η_c	CAU's compressor efficiency
η_t	CAU's turbine efficiency
η_{mc}	CAU's compressor mechanical efficiency
η_{mt}	CAU's turbine mechanical efficiency
T_{inH2I}	temperature of the hydrogen boil-off at the primary heat exchanger's inlet (K)
$T_{outH2II}$	temperature of the hydrogen boil-off at the secondary heat exchanger's exit (K)
T_{inH2II}	temperature of the hydrogen boil-off at the secondary heat exchanger's inlet (K)
T_{rec}	recovery temperature (K)
T_w	wall temperature (K)
T_∞	free stream air temperature (K)
v_∞	free stream velocity (m/s)
w_{H2}	hydrogen boil-off speed in the convective insulation layer (m/s)
w_{air}	air speed in the convective insulation layer (m/s)

Acronyms

ATR	air turbo rocket
C	compressor
CAU	cold air unit
CMC	ceramic matrix composite
DMR	dual mode ramjet
ECS	environmental control system
LH2	liquid hydrogen
MEA	more electric aircraft
PHE	primary heat exchanger
SAFs	sustainable aviation fuels
SHE	secondary heat exchanger
T	turbine
TCS	thermal control system
TEMS	thermal and energy management system
TPS	thermal protection system
WS	water separator

References

1. Viola, N.; Roncioni, P.; Gori, O.; Fusaro, R. Aerodynamic Characterization of Hypersonic Transportation Systems and Its Impact on Mission Analysis. *Energies* **2021**, *14*, 3580. [CrossRef]
2. Viola, N.; Fusaro, R.; Gori, O.; Marini, M.; Roncioni, P.; Saccone, G.; Saracoglu, B.; Ispir, A.C.; Fureby, C.; Nilson, T.; et al. STRATOFLY MR3—How to reduce the environmental impact of high-speed transportation. In Proceedings of the AIAA Scitech 2021 Forum, Virtual, 19–21 January 2021; pp. 1–21.
3. Ferretto, D.; Fusaro, R.; Viola, N. Innovative Multiple Matching Charts approach to support the conceptual design of hypersonic vehicles. *Proc. Inst. Mech. Eng. Part G J. Aerosp. Eng.* **2020**, *234*, 1893–1912. [CrossRef]
4. Moir, I.; Seabridge, A. *Aircraft Systems: Mechanical, Electrical, and Avionics Subsystems Integration*, 3rd ed.; John Wiley & Sons: Hoboken, NJ, USA, 2008.
5. Cheng, K.; Qin, J.; Sun, H.; Dang, C.; Zhang, S.; Liu, X.; Bao, W. Performance assessment of an integrated power generation and refrigeration system on hypersonic vehicles. *Aerosp. Sci. Technol.* **2019**, *89*, 192–203. [CrossRef]
6. Hank, J.; Murphy, J.; Mutzman, R. The X-51A Scramjet Engine Flight Demonstration Program. In Proceedings of the 15th AIAA International Space Planes and Hypersonic Systems and Technologies Conference, Dayton, OH, USA, 28 April–1 May 2008; Volume 2540. [CrossRef]
7. Zhang, D.; Qin, J.; Feng, Y.; Ren, F.; Bao, W. Performance evaluation of power generation system with fuel vapor turbine onboard hydrocarbon fueled scramjets. *Energy* **2014**, *77*, 732–741. [CrossRef]
8. Cheng, K.; Qin, J.; Sun, H.; Dang, C.; Zhang, S.; Liu, X.; Bao, W. Performance assessment of a closed-recuperative-Brayton-cycle based integrated system for power generation and engine cooling of hypersonic vehicle. *Aerosp. Sci. Technol.* **2019**, *87*, 278–288. [CrossRef]
9. Fusaro, R.; Vercella, V.; Ferretto, D.; Viola, N.; Steelant, J. Economic and environmental sustainability of liquid hydrogen fuel for hypersonic transportation systems. *CEAS Space J.* **2020**, *12*, 441–462. [CrossRef]
10. Steelant, J. Achievements Obtained for Sustained Hypersonic Flight within the LAPCAT project. In Proceedings of the 15th AIAA International Space Planes and Hypersonic Systems and Technologies Conference, Dayton, OH, USA, 28 April–1 May 2008.
11. Steelant, J.; Varvill, R.; Walton, C.; Defoort, S.; Hannemann, K.; Marini, M. Achievements Obtained for Sustained Hypersonic Flight within the LAPCAT-II project. In Proceedings of the 20th AIAA International Space Planes and Hypersonic Systems and Technologies Conference, Glasgow, UK, 6–9 July 2015.
12. Rehfeld, N.; Berton, B.; Diaz, F.; Tanaka, T.; Morita, K.; Kimura, S. JediAce: Japanese-European De-Icing Aircraft Collaborative Exploration. In Aviation in Europe—Innovating for Growth. In Proceedings of the Seventh European Aeronautics Days, London, UK, 20–22 October 2015. [CrossRef]
13. Voland, R.T.; Huebner, L.D.; McClinton, C.R. X-43A Hypersonic vehicle technology development. *Acta Astronaut.* **2006**, *59*, 181–191. [CrossRef]
14. Adolf, J.; Balzer, C.H.; Louis, J.; Schabla, U.; Fischedick, M.; Arnold, K.; Schüwer, D. *Energy of the Future? Sustainable Mobility through Fuel Cells and H2*; Shell Hydrogen Study; Wuppertal Institute: Wuppertal, Germany, 2017.
15. IGEM. Hydrogen Powered Aviation: A fact-based study of hydrogen technology, economics, and climate impact by 2050. In *Fuel Cell and Hydrogen Joint Undertaking*; IGEM: Boston, MA, USA, 2020.
16. Grewe, V.; Stenke, A.; Plohr, M.; Korovkin, V.D. Climate functions for the use in multi-disciplinary optimization in the pre-design of supersonic business jet. *Aeronaut. J.* **2010**, *114*, 259–269. [CrossRef]
17. Grewe, V.; Plohr, M.; Cerino, G.; Di Muzio, M.; Deremaux, Y.; Galerneau, M.; Martin, P.D.S.; Chaika, T.; Hasselrot, A.; Tengzelius, U.; et al. Estimates of the climate impact of future small-scale supersonic transport aircraft – results from the HISAC EU-project. *Aeronaut. J.* **2010**, *114*, 199–206. [CrossRef]
18. Grewe, V.; Stenke, A.; Ponater, M.; Sausen, R.; Pitari, G.; Iachetti, D.; Rogers, H.; Dessens, O.; Pyle, J.; Isaksen, I.; et al. Climate impact of supersonic air traffic: An approach to optimize a potential future supersonic fleet – results from the EU-project SCENIC. *Atmos. Chem. Phys.* **2007**, *7*, 5129–5145. [CrossRef]
19. Terrenoire, E.; Hauglustaine, D.; Gasser, T.; Penanhoat, O. The contribution of carbon dioxide emissions from the aviation sector to future climate change. *Environ. Res. Lett.* **2019**, *14*, 84019. [CrossRef]
20. Hauglustaine, D.A.; Koffi, B. Boundary layer ozone pollution caused by future aircraft emissions. *Geophys. Res. Lett.* **2012**, *39*, 13808. [CrossRef]
21. Koffi, B.; Szopa, S.; Cozic, A.; Hauglustaine, D.; van Velthoven, P. Present and future impact of aircraft, road traffic and shipping emissions on global tropospheric ozone. *Atmos. Chem. Phys.* **2010**, *10*, 11681–11705. [CrossRef]
22. Hoor, P.; Borken-Kleefeld, J.; Caro, D.; Dessens, O.; Endresen, O.; Gauss, M.; Grewe, V.; Hauglustaine, D.; Isaksen, I.S.A.; Jöckel, P.; et al. The impact of traffic emissions on atmospheric ozone and OH: Results from QUANTIFY. *Atmos. Chem. Phys.* **2009**, *9*, 3113–3136. [CrossRef]
23. Hauglustaine, D.A.; Hourdin, F.; Walters, S.; Jourdain, L.; Filiberti, M.-A.; Larmarque, J.-F. Holland, Interactive chemistry in the Laboratoire de Météorologie Dynamique general circulation model: Description and background tropospheric chemistry evaluation. *Geophys. Res. Lett.* **2004**, *109*, D04314. [CrossRef]
24. Fusaro, R.; Ferretto, D.; Viola, N.; Villace, V.F.; Steelant, J. A methodology for preliminary sizing of a Thermal and Energy Management System for a hypersonic vehicle. *Aeronaut. J.* **2019**, *123*, 1508–1544. [CrossRef]
25. Cronin, M.J. Design Aspects of Systems in All-Electric Aircraft. *SAE Techn. Pap. Ser.* **1982**, *91*, 821158–821559. [CrossRef]

26. Villace, V.F.; Steelant, J. The Thermal Paradox of Hypersonic Cruisers. In Proceedings of the 20th AIAA International Space Planes and Hypersonic Systems and Technologies Conference, Glasgow, UK, 6–9 July 2015; p. 14.
27. Langener, T.; Erb, S.; Steelant, J. Trajectory Simulation and Optimization of the LAPCAT MR2 Hypersonic Cruiser Concept. In Proceedings of the 29th Congress of the International Council of the Aeronautical Sciences, St. Petersburg, Russia, 7–12 September 2014.
28. Cengel, Y.A. *Introduction to Thermodynamics and Heat Transfer*; McGraw Hill Book Co.: New York, NY, USA, 2010.
29. Ferretto, D.; Fusaro, R.; Viola, N. A conceptual design tool to support high-speed vehicle design. In *AIAA Aviation 2020 Forum*; American Institute of Aeronautics and Astronautics: Reston, VA, USA, 2020; p. 22.
30. Fusaro, R.; Ferretto, D.; Viola, N. Model-Based Object-Oriented systems engineering methodology for the conceptual design of a hypersonic transportation system. In Proceedings of the 2016 IEEE International Symposium on Systems Engineering (ISSE), Edinburgh, UK, 3–6 October 2016; pp. 1–8. [CrossRef]
31. Fusaro, R.; Ferretto, D.; Viola, N. MBSE approach to support and formalize mission alternatives generation and selection processes for hypersonic and suborbital transportation systems. In Proceedings of the 2017 IEEE International Systems Engineering Symposium (ISSE), Vienna, Austria, 11–13 October 2017; pp. 1–8. [CrossRef]
32. De Vita, F.; Viola, N.; Fusaro, R.; Santoro, F. Assessment of Hypersonic Flights Operation Scenarios: Analysis of Launch and Reentry Trajectories, and Derived Top Level Vehicle System and Support Infrastructure Concepts and Requirements. In Proceedings of the 20th AIAA International Space Planes and Hypersonic Systems and Technologies Conference, Glasgow, UK, 6–9 July 2015.
33. Mammarella, M.; Paissoni, C.; Viola, N.; Denaro, A.; Gargioli, E.; Massobrio, F. The Lunar Space Tug: A sustainable bridge between low Earth orbits and the Cislunar Habitat. *Acta Astronaut.* **2017**, *138*, 102–117. [CrossRef]